SCIENCE CHINA Materials

REVIEWS

mater.scichina.com link.springer.com

Published online 19 May 2020 | https://doi.org/10.1007/s40843-020-1305-6

Sci China Mater 2020, 63(11): 2089–2118

SPECIAL TOPIC: Advanced Photocatalytic Materials

Oxygen vacancies in metal oxides: recent progress towards advanced catalyst design

Guoxin Zhuang[1,2], Yawen Chen[1,2], Zanyong Zhuang[1,2*], Yan Yu[1,2*] and Jiaguo Yu[3*]

ABSTRACT **Energy crisis and environmental problems urgently drive the proposal of new strategies to improve human wellbeing and assist sustainable development. To this end, scientists have explored many metal oxides-based photocatalysts with high stability, low cost, earth abundance, and potentially high catalytic activity relevant for key applications such as H_2O splitting, CO_2 reduction, N_2 fixation, and advanced oxidation of pollutants. In these metal oxides, oxygen vacancies (OVs) are ubiquitous and intrinsic defects with pronounced impacts on the physicochemical properties of the catalysts, which may open new opportunities for obtaining efficient metal oxides. The thorough understanding of the structural and electronic nature of OVs is necessary to determine how they serve as catalytically active sites. In this review, we summarize the origin of OVs, the strategies to introduce OVs, as well as the fundamental structure-activity relationships to relate these crystal defects to catalyst properties including light absorption, charge separation, etc. We emphasize the mechanism of OVs formation and their effects on the intrinsic catalytic characteristics of the metal oxides. We also present some multicomponent catalytic platforms where OVs contribute to catalysis *via* synergy. Finally, opportunities and challenges on engineering defects in photocatalysts are summarized to highlight the future directions of this research field.**

Keywords: oxygen vacancy, catalysis, defect engineering, energy and environment, metal oxide

INTRODUCTION

As a result of population growth and the process of industrialization, fossil fuels including coal, oil, and natural gas are being rapidly consumed, which gives rise to environmental issues like the emission of greenhouse gases and the discharge of hazardous waste. Technologies for safe and clean energy are desired to cut back the rising consumption of fossil fuels. Consequently, sunlight-driven catalytic reactions relevant for a myriad of applications such as H_2O splitting, CO_2 reduction, N_2 fixation, and advanced oxidation of pollutants, all meaningful for improving the wellbeing of mankind and ensuring the sustainable development of the society, have gained increasing attention. To this end, many metal oxides-based photocatalysts (e.g., TiO_2 [1–7], ZnO [8,9], MoO_3 [10,11], CuO [12–15], MnO_2 [16,17], VO_2 [18], WO_3 [19], and CoO_x [20]) have been explored, owing to their high stability, low cost, abundance in the Earth, and appealing catalytic activity. It is well acknowledged that both high catalytic efficiency and high selectivity are indispensible for photocatalytic reactions to industrial application. Despite decades of research exploring advanced photocatalysts, as of today the development of economic and efficient catalysts remains challenging in both fundamental research and practical applications. The efficiency of photocatalyst reported is often limited by the inadequate absorption of visible light, excessive charge recombination, as well as the poor reactivity of the so-called inert molecules (e.g., CO_2, N_2) in cataltyic reactions.

Point defects such as oxygen vacancies (OVs) are ubiquitous in metal oxides, have a pronounced effect on the physical and chemical properties of the material, and thus open new opportunities for obtaining efficient metal oxide catalysts [21–23]. The concept of OV was proposed in the 1960s by Tompkins *et al.* [24], in which OV was supposed to be a kind of species in solid superficial chemistry. Subsequently, OV was found to exist in many

[1] College of Materials Science and Engineering, Fuzhou University, Fuzhou 350108, China
[2] Key Laboratory of Advanced Materials Technologies (Fuzhou University), Fujian Province University, Fuzhou 350108, China
[3] State Key Laboratory of Advanced Technology for Materials Synthesis and Processing, Wuhan University of Technology, Wuhan 430070, China
* Corresponding authors (emails: zyzhuang@fzu.edu.cn (Zhuang Z); yuyan@fzu.edu.cn (Yu Y); jiaguoyu@yahoo.com (Yu J))

oxides and account for their distinct physicochemical properties (e.g., optical properties [25,26] and electrical conduction [27,28]) with reference to stoichiometric oxides. Some studies focused on the production of OVs [29] and the diffusion of OVs in oxides [30,31]. Extensive studies on OVs started from 2000 when researchers found that OVs could act as active sites in catalytic reactions to adsorb substrates [32,33]. In the study on black TiO_2, researchers further found that OVs played critical roles in boosting the solar absorption of oxides [34]. Since then enormous efforts have been devoted to the regulation of OVs for advanced photocatalysis [35–37], electrocatalysis, [38,39] and thermal catalysis [40,41].

To date, the nature and content of OVs in metal oxides have been shown to directly affect catalyst functions in reactions including H_2 evolution [42–44], NO reduction [12], CO oxidation [45,46], C_6H_5Cl destruction [47], etc. Prior studies have revealed that OVs improve the catalytic performance mainly by modulating light absorption [48], charge transfer [49–52], molecular fixation [21], and/or catalyst conductivity [53,54]. Several aspects should be considered when evaluating the impact of OVs on the photocatalyst. For example, sometimes OVs serve as charge separation centers to improve carrier separation efficiency. Huo *et al.* [55] found that OVs-rich Bi_2WO_6 allowed stronger photocatalytic NO oxidation compared with its stoichiometric counterpart. From density functional theory (DFT) calculations, they found that a new defect level associated with OVs was generated near the Fermi level, which increased the photoabsorption and electronic conductivity, suppressed the recombination of electron–hole, and prolonged the lifetime of carriers. OVs may also create unsaturated coordination sites (e.g., edge, corner, or terrace), which are more suitable for reactions such as H_2 evolution and CO_2 reduction to take place. As of now, the intrinsic functions of OVs on catalytic reaction remain elusive and controversial, which hinders the strategic rational design of catalyst defect. What is worse, the introduction of OVs to metal oxides is hard to control. OVs in catalysts have been generated by (i) thermal treatment under vacuum or in an inert atmosphere (He, N_2, and Ar), (ii) chemical reduction, (iii) ion doping, and (iv) interfacial engineering, and many of these processes require tedious procedures with demanding precision under particular time, temperature, and pressure. A thorough understanding of the controllable regulation of OVs and the mechanisms of defect-modulated photocatalysis is imperative for effective catalyst design [56–58]. A comprehensive review of the state-of-the-art in the regard will help promote further developments in this important, fascinating, and burgeoning research area.

In this review, we summarize the primary origin and controllable regulation of OVs in various metal oxides, to assist the rational design of high-performance OV-mediated catalysts. We list the viable strategies to control the OVs in photocatalysts and present the principle of OVs formation. We put special emphasis on tuning the electronic structures of oxygen-deficient metal oxide photocatalysts to manipulate their performance in light absorption, charge carrier transfer and separation, molecule capture and activation, and all effects on the eventual thermodynamics of the catalytic reactions. We reveal the structure-function relationship of OVs in OVs-mediated catalytic applications such as pollutant degradation, air purification, H_2 production, and CO_2 reduction. Finally, challenges and prospects are presented.

ORIGIN OF OVs

Lattice O atoms from oxides can either directly enter the gas phase in the form of O_2 (i.e., overflow) or be chemically reduced to form OVs in the solid phase. Ye *et al.* [59] systematically investigated different conditions that led to the formation of OVs at different sites on the In_2O_3 (110) surface (Table 1). The lattice O atoms can either directly desorb to form O_2 or react with H_2 or CO to form H_2O or CO_2.

$MO_2 \rightarrow MO_{2-x} + \frac{1}{2}x\ O_2\ (g)$.

The OVs change the perfect periodic arrangement of the crystal (Fig. 1) as well as the electronic structure around the OVs [60]. Hence, the electronic charge asso-

Table 1 Reaction energy (in eV) of OV creation on the In_2O_3 (110) surface in different sites (D1, D2, D3, D4, D5 and D6) by thermal desorption and by reduction. Adapted with permission from Ref. [59], Copyright 2013, American Chemical Society.

Reaction equation	ΔE					
	D1	D2	D3	D4	D5	D6
[a] p-In_2O_3(110) → OV-In_2O_{3-x}(110) + ½ O_2	1.96	1.98	2.35	2.47	2.40	2.14
[b] p-In_2O_3(110) + H_2 → OV-In_2O_{3-x}(110) + H_2O	−0.57	−0.56	−0.19	−0.07	−0.13	−0.40
[c] p-In_2O_3(110) + CO → OV-In_2O_{3-x}(110) + CO_2	−1.30	−1.28	−0.91	−0.79	−0.86	−1.12

a) Thermal decomposition; b) H_2 reduction; c) CO reduction.

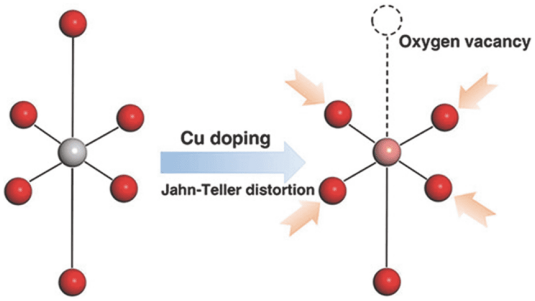

Figure 1 Polyhedral representation of a pristine TiO_6 octahedron and a defective octahedron with OV resulting from Cu doping at a Ti site. Adapted with permission from Ref. [60], Copyright 2019, WILEY-VCH Verlag GmbH & Co. KGaA, Weinheim.

ciated with the departed O atom (i.e., $2e^-$) will redistribute to the surrounding lattice. Because metal oxides have multiple oxidation states, the resulting extra electron density localizes primarily on the neighboring cations, reducing them to a lower valence state [61]. Theoretical calculations demonstrate that abundant localized electrons will form at the OVs, which affect the physical and chemical property of metal oxides (e.g., optical characteristics, electron transport, surface structure, etc.) and provide active sites for catalysis. In addition, OVs on the surface can strongly attract reactive molecules and thus change their state. These effects altogether improve the catalytic performance of the metal oxides that possess OVs. To facilitate the design and modification of catalysts, it is essential to understand in-depth how OVs are generated, determine various strategies to regulate OVs, and rationalize the effects of OVs on both the catalyst itself and the reaction. The following chapter summarizes different strategies suitable for generating and manipulating OVs.

STRATEGIES TO CREATE OVs

Numerous synthetic strategies have been developed to create OVs in metal oxides, e.g., high-energy particle bombardment, high-temperature calcination, chemical reduction, ion doping, and tuning the heterostructure interface, all of which facilitate the escape of O atoms. Many syntheses require harsh conditions (e.g., high temperature, anaerobic conditions, etc.) yet allow limited control of the resulting OVs and cannot be readily generalized. Uncovering how OVs are generated behind the common operational parameters is indispensable, because photocatalytic materials with clearly defined OVs must be obtained before researchers can evaluate the relationship between defects and photocatalytic performance and then establish the related reaction mechanisms.

High-energy particle bombardment (HEPB)

Many studies over past decades have reported that HEPB offers a promising way to create OVs in metal oxides, and a possible mechanism of OVs formation *via* HEPB is also proposed [21,62–72]. High-energy particles suitable for HEPB could be electrons, protons, or ions that can preferentially seize and desorb lattice oxygen on the surface of oxides. In this way, HEPB induces an overflow of oxygen from the lattice and generates OVs [21]. To date, HEPB has successfully produced a myriad of oxygen-deficient metal oxides, including Co_3O_4 [21,62], ZnO [63,73,74], $SnCo_{0.9}Fe_{0.1}(OH)_6$ [64], CeO_2 [65,75], TiO_2 [76–78], SnO_2 [67,79], $SrTiO_3$ [68], SiO_2 [69] and Fe_2O_3 [70,80]. Knotek and Feibelman [81] found that the electrons with energy higher than 34 eV can desorb surface oxygen through an interatomic Auger recombination process. von Soosten *et al.* [82] suggested that the high-energy particles with energy over tens of eV would induce loosely bound O atom to overflow from the surface. In the case of ZnO, Park *et al.* [63] further revealed that high-energy proton tended to interact with oxygen anions than metal cations, and in that case, HEPB normally created OVs rather than cation vacancies in ZnO (Fig. 2a). Furthermore, the oxygen atoms weakly bound to the cations that have fewer charges or larger ion radius (e.g., Zn^{2+}, In^{3+}) are more likely to be released from the lattice [83]. The advantage of HEPB in creating defects is that the bombardment with particles of appropriate energy intensity produces OVs without incurring unwanted damages to the surface. Moreover, the concentration of OVs can be regulated by adjusting the treatment time, the irradiation particle, and the intrinsic structure of the metal oxide. For instance, Xu *et al.* [62] designed an OVs-rich Co_3O_4 *via* a one-step plasma-engraving strategy. The Co_3O_4 nanosheets array were treated by Ar plasma (commercial 13.56 MHz RF source, 100 W power and 40 Pa pressure) with treatment time varying from 0 to 60, 120, 180, and 240 s. Gratifyingly, the Co_3O_4 engraved for 120 s contained a suitable amount of OVs and displayed the highest catalytic performance. It must be noted that not all high-energy particles are effective for generating OVs. Chen *et al.* [66] demonstrated that whereas Ar plasma creates OVs in NiO/TiO_2, O_2 or CO_2 plasma does not work under identical condition. Kim and coworkers [63] also proved that under the same dose of proton irradiation, amorphous zinc tin oxide (α-ZTO), amorphous indium gallium zinc oxide (α-IGZO), and crystalline zinc oxide (ZnO) produced different concentrations of OVs, and the concentration also differed when the dose of proton irradiation varied (Fig. 2b–e).

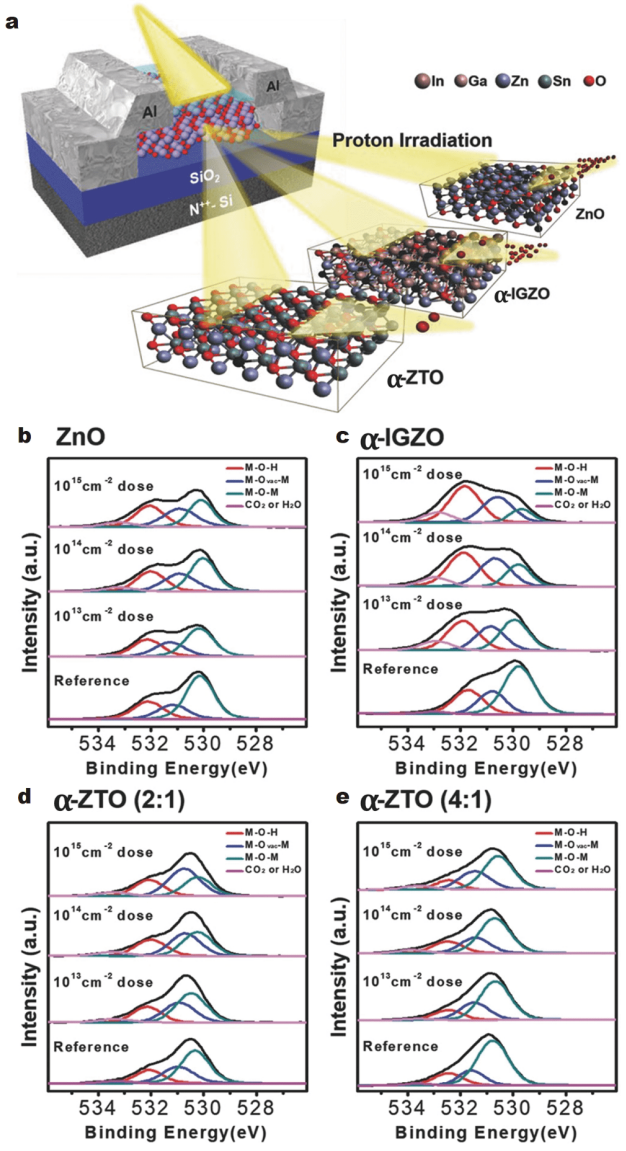

Figure 2 (a) Schematic of high-energy proton irradiation on oxide-semiconductor thin-film transistors (α-ZTO, α-IGZO, and ZnO); the O 1s spectra from X-ray photoelectron spectroscopy (XPS) analysis are given for (b) ZnO, (c) α-IGZO, (d) α-ZTO (2:1), and (e) α-ZTO (4:1) before and after various doses of proton irradiation. Adapted with permission from Ref. [63], Copyright 2018, WILEY-VCH Verlag GmbH & Co. KGaA, Weinheim.

Thermal treatment

Alternatively, calcination of samples at high temperature in an oxygen-deficit atmosphere also creates OVs [84]. During calcination at high temperature, the surface atoms vibrate violently, and the surface lattice oxygen can easily diffuse and overflow [85–88].

Experimental parameters like heating temperature and time generally play critical roles in tailoring the concentration of OVs obtained after calcination. Higher temperature and extended heating time normally increase the concentration of OVs [89,90]. For instance, Tan *et al.* [91] found that $SrTiO_3$ annealed at 375°C had higher concentration of OVs compared with the samples annealed at 300°C, and extending the heating time from 30 to 60 min further assisted OVs formation. Likewise, Jaiswar *et al.* [92] demonstrated that annealing $CaMn_7O_{12}$ at 970°C created more OVs when the heating time was increased from 12 to 15 h. Nevertheless, there are also exceptions. For example, Jiang *et al.* [93] observed that the concentration of OVs in Co_3O_4 decreased when the annealing temperature was increased from 350 to 700°C, and reasoned that Co_3O_4 suffered from pyrolysis at high temperature.

The effects of the atmosphere and pressure on the generation of OVs during calcinations are increasingly appreciated in recent years. Hypoxic atmosphere (e.g., vacuum [94–96], He [97], Ar [85], and N_2 [98]) facilitates the formation of OVs. In case of annealing VO_2 film in Ar atmosphere, Xu *et al.* [85] found that increasing the Ar pressure generated a larger number of OVs, and also observed a shift of the V $2p_{3/2}$ peak to a lower binding energy. Vacuum tends to create more OVs at a relatively low temperature [96,97,99,100]. Liu *et al.* [96] found that the amount of OVs in the annealed SnO_{2-x}/In_2O_{3-y} increased when the annealing was carried out in an ultra-high vacuum (UHV) system instead of a furnace annealing system (Fig. 3). In fact, a hypoxic atmosphere is desired but not mandatory. For example, Bao *et al.* [39] demonstrated that annealing $NiCo_2O_4$ nanosheets in air created OVs-rich NiCo hydroxides, and the amount of OVs reduced sharply when the same process was carried out in O_2 atmosphere.

Chemical reduction

Although the abovementioned methods efficiently create OVs, they cannot activate the lattice oxygen at low temperature, which hinders deliberate control in generating OVs. In contrast, the chemical reduction of metal oxides by chemical agents (e.g., H_2 [31], NH_3 [101], $NaBH_4$ [102]) could produce OVs at relatively low temperature. The reductive molecules are firstly adsorbed on the surface of metal oxides, and then grab O atoms through electron transfer to the surface oxygen and thus generate OVs. Hydrogenation is currently the most popular pathway in chemical reduction [101,103–105].

Ye *et al.* [59] found that the reductive H_2 atmosphere modulates the thermodynamics and the temperature required for creating OVs on In_2O_3. They showed with DFT

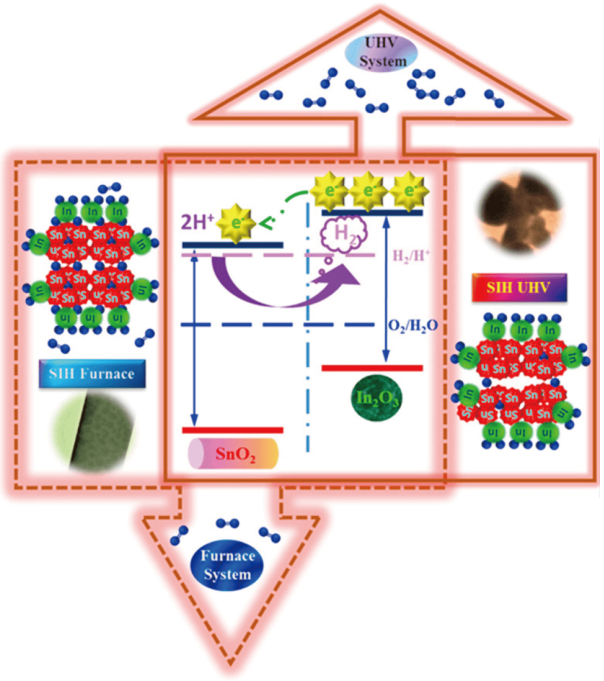

Figure 3 Schematic and structure of SnO_{2-x}/In_2O_{3-y} prepared from UHV (solid) and furnace annealing (dotted) system, with O atom in blue. Adapted with permission from Ref. [96], Copyright 2018, Elsevier.

calculations that a redox reaction between H_2 and the O atoms of In_2O_3 to form H_2O and OVs was intrinsically exothermic, with the formation energy (E_V) of OVs being −0.57 eV (Table 1). In contrast, Bielz *et al.* [106] previously created OVs on In_2O_3 at ~673 K by calcination, but Ye *et al.* [59] could create OVs at a relatively lower temperature of 340 K with the presence of H_2. Note that temperature also determines the concentration and type of OVs. Zhu *et al.* [107–109] adopted H_2 reduction to control the concentration and type of OVs on the surface of $BiPO_{4-x}$. When the temperature is set below 270°C, most OVs reside on the surface of $BiPO_{4-x}$. The concentration of OVs gradually increases with rising temperature, and over 300°C, both surface and bulk OVs are created. The oxygen-deficient $BiPO_{4-x}$ with surface OVs has higher photocatalytic activity than the $BiPO_{4-x}$ rich in bulk OVs.

Ammonia (NH_3) is another commonly used reducing agent. Thanks to its weakly reducing reactivity, NH_3 helps create OVs in transition metal oxides (TMOs) during the nitridation process. A possible mechanism was proposed by Liu *et al.* [101], who demonstrated when WO_3 was treated with NH_3, both the H and N atoms of NH_3 can seize O atoms from WO_3, to form H_2O, N_2, N_2O, and NO and reduce WO_3 to OVs-rich WO_{3-x} (Fig. 4). Analogously, Wang *et al.* [110] presented a universal low-temperature ammonia reduction method to prepare OV-enriched TMOs without N-doping. For example, they prepared OVs-rich TiO_2 by heating commercial P25-TiO_2 in flowing NH_3 [110,111]. Maqbool *et al.* [112] also created black anatase TiO_2 rich in OVs by NH_3 reduction. According to the diffuse reflectance UV-vis-NIR spectroscopy, the obtained OVs-rich TiO_2 shows an absorption that not only covers visible light but also extends well into the NIR. In contrast, the pristine TiO_2 can only respond to ultraviolet irradiation.

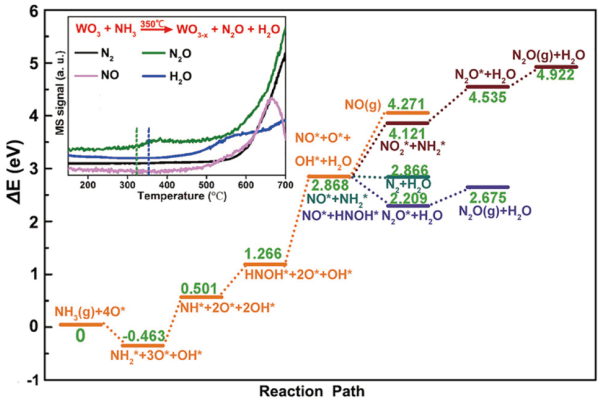

Figure 4 Calculated reaction energy diagram of NH_3 treatment over the WO_3 (001) plane, along with mass spectrometer signals (online MS signals) of N_2, NO, H_2O, and N_2O generated from the temperature-programmed reaction of WO_3 with NH_3. Adapted with permission from Ref. [101], Copyright 2019, Elsevier.

The reduction of metal oxides can also take place in the liquid phase. The reduction in the liquid phase enables large scale modification of oxides under mild condition, and the OVs concentration can be readily manipulated by adjusting the dose of reducing agent, the reaction temperature, and time [113]. Thus far, OVs-rich Co_3O_4 [114], Bi_2WO_6 [115], and Bi_4MoO_9 [102] have been prepared by $NaBH_4$ reduction at room temperature in the liquid phase. Intriguingly, substantial OVs are created in Bi_4MoO_9/Bi^0 by only stirring the precursor in aqueous $NaBH_4$ [102]. Yang *et al.* [116] integrated perovskite $La_{0.8}Sr_{0.2}CoO_3$ (OM LSCO) catalysts that had an ordered macroporous structure into commercial cordierite without adhesives by *in situ* solution assembly and then created OVs on the resulting material by $NaBH_4$ reduction to give OVs-OM LSCO (Fig. 5a). The presence of OVs is clearly established by XPS and electron paramagnetic resonance (EPR) (Fig. 5b–e). The OVs-OM LSCO has significantly enhanced activity for low-temperature CO oxidation because the ordered macroporous framework endows the perovskite with a high degree of accessible reactive surface and the engineered OVs notably im-

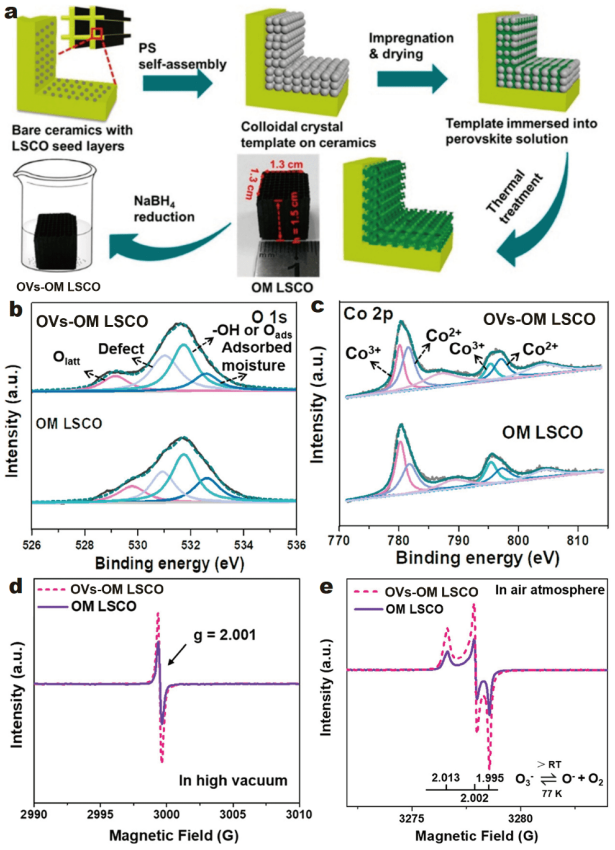

Figure 5 (a) Schematic illustration of the fabrication process of OVs-OM LSCO; (b) O 1s and (c) Co 2p XPS spectra of OVs-OM LSCO and OM LSCO; low-temperature EPR spectra of OVs-OM LSCO and OM LSCO (d) in high vacuum and (e) in air. Adapted with permission from Ref. [116], Copyright 2019, American Chemical Society.

proves the abundance of monatomic oxygen ions (O^-).

OVs can also be created when the metal oxide is treated in a weakly reducing alcohol solution [117,118]. Bai *et al.* [119] introduced OVs to Bi_5O_7I nanosheets by stirring the precursor in a mixed solvent containing ethylene glycol and ethanol. The ethylene glycol is believed to reduce the surface oxygen atoms of Bi_5O_7I because the oxygen density is high on the (001) surface of Bi_5O_7I. Cai *et al.* [120] successfully produced OVs on the (111) surface of Co_3O_4 *via* the solvothermal reduction of Co_3O_4 in ethylene glycol under alkaline condition. In general, the advantages of solution or solvent-based strategies include room-temperature processing, shorter reaction time, controllability, versatility, and scalability.

Ion doping

As a conventional tool to tune the chemical composition and properties of functional materials, ion doping also could produce OVs because the dopant always destroys the long-term periodic order of the lattice oxygen in the oxide. For instance, OVs will be created to maintain the electrostatic balance when a low valence M^{3+} dopant is incorporated into MO_2 [121–128]. The dopant ion with a low valence state subsequently substitutes the original metal nodes in the oxide, and as a result, OVs are formed to rebalance the charge. For example, OVs are needed when a La^{3+} ion serves as a dopant to substitute Ce^{4+} in CeO_2 [129]. Similarly, Wang *et al.* [130] found that the Ni-doped $La_{0.8}Sr_{0.2}Mn_{1-x}Ni_xO_3$ had more OVs than the undoped $La_{0.8}Sr_{0.2}MnO_3$. Ion exchange is a facile means to implement doping and thus regulate OVs. For instance, OVs-rich NiO nanorods have been created from a ZnO precursor by ion exchange with Ni^{2+} [131], and OVs-rich CoO is also produced from ZnO by ion exchange with Co^{2+} [132].

Theoretical studies have been performed to reveal how the dopants affect the formation of OVs. From DFT calculations, Nolan *et al.* [61,98,129,133] suggested that compared with the undoped counterparts, the doped materials can produce OVs more easily because low valence metal dopant led to a lower E_V. The E_V of ramsdellite-MnO_2 doped with Zn is −0.90 and −0.57 eV on the (110) and (010) surfaces, much lower than that of the undoped ramsdellite-MnO_2 (0.22 and 0.76 eV respectively) [134]. Wang *et al.* [133] also found that the first OV formed in Cu^{2+}-doped CeO_2 was spontaneous thanks to the charge compensation. The presence of first OV then expedited the formation of the second and third OVs, and the E_V reduced from 1.82 eV for the first OV to 1.65 eV for the third OV (Fig. 6). These OVs tend to be generated near the Cu sites, indicating that the O atom adjacent to the doped cation is more labile to overflow [135].

Apart from cation doping, anion doping (e.g., with N, C, and S) may also contribute to the formation of OVs [9,136–139]. For instance, Li *et al.* [140] designed OVs-rich Co_3O_4 and CoO by doping P anions *via* controlled calcination of cobalt–alanine complexes. Sun *et al.* [141] used gaseous sulfur treatment to create OVs on the surface of $Li_{1.2}Ni_{0.13}Co_{0.13}Mn_{0.54}O_2$ (LNCMO@S) uniformly by replacing oxygen with S atoms (Fig. 7). Instead of resorting to conventional calcination, Sun *et al.* [142] adopted a facile ionic liquid strategy to dope N, P, and F into $CoFe_2O$ to create abundant OVs. Unfortunately, compared with cation doping, the mechanism of generating OVs by anion doping is much less investigated.

Interfacial engineering

Adjusting the heterostructure interface further assists

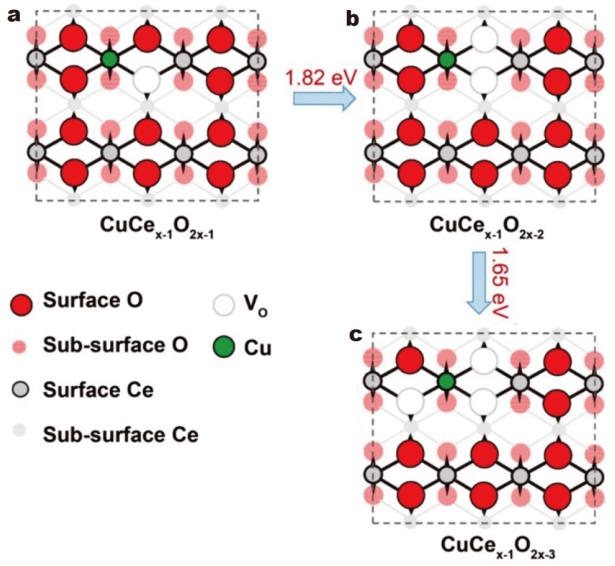

Figure 6 Theoretical calculations of the most stable structures and E_V of CeO_2 (110) doped with one single Cu site with (a) 1 OV; (b) 2 OVs; and (c) 3 OVs. Adapted with permission from Ref. [133], Copyright 2018, American Chemical Society.

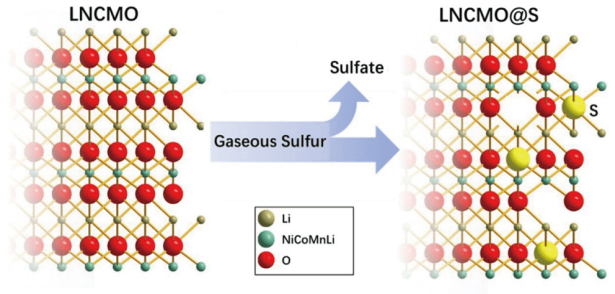

Figure 7 Creating OVs by the partial replacement of O by S *via* anion doping after gaseous sulfur treatment of $Li_{1.2}Ni_{0.13}Co_{0.13}Mn_{0.54}O_2$ (LNCMO). Adapted with permission from Ref. [141], Copyright 2019, Elsevier.

OVs formation [143–145]. Lately, Nolan *et al.* [146,147] found that the formation of point defects such as OVs was significantly more favorable in the heterojunction of mixed-phase TiO_2 than in single-phase TiO_2. Along with newly added OVs, electrons are localized into low coordinated Ti sites in the interfaces, thus creating special active sites in mixed-phase TiO_2. Abundant OVs are often found close to grain boundaries or heterojuctions [19], because the E_V is always dependent on the position [146,148]. For example, the $LaAlO_3/SrTiO_3$ interface has much smaller E_V than the surface of $LaAlO_3$ [148]. Focusing on polytype TiO_2, Nolan *et al.* [146] performed DFT calculations to probe the effect of the rutile–anatase TiO_2 interface on defect formation. They found that the interfacial region was disordered and contained low coordinated Ti sites and abundant OVs. Qiu *et al.* [149] designed a built-in p–n heterojunction that combined catalytically inactive CeO_2 with Co_3O_4 to construct CeO_2/Co_3O_4 (Fig. 8a). Substantial OVs are formed by the strongly coupled heterojunction interface according to XPS (Fig. 8c–f), and they allow rapid interfacial charge transfer from CeO_2 to Co_3O_4 (Fig. 8b), which improves the catalytic performance of the heterojunction. Veal *et al.* [150] distributed OVs in $In_2O_3/ZrO_2/Y_2O_3$ heterostructured oxides with reversible control of the OVs concentration. The redistribution of oxygen ions across the heterointerface is induced by an applied electric field oriented in the plane of the interface.

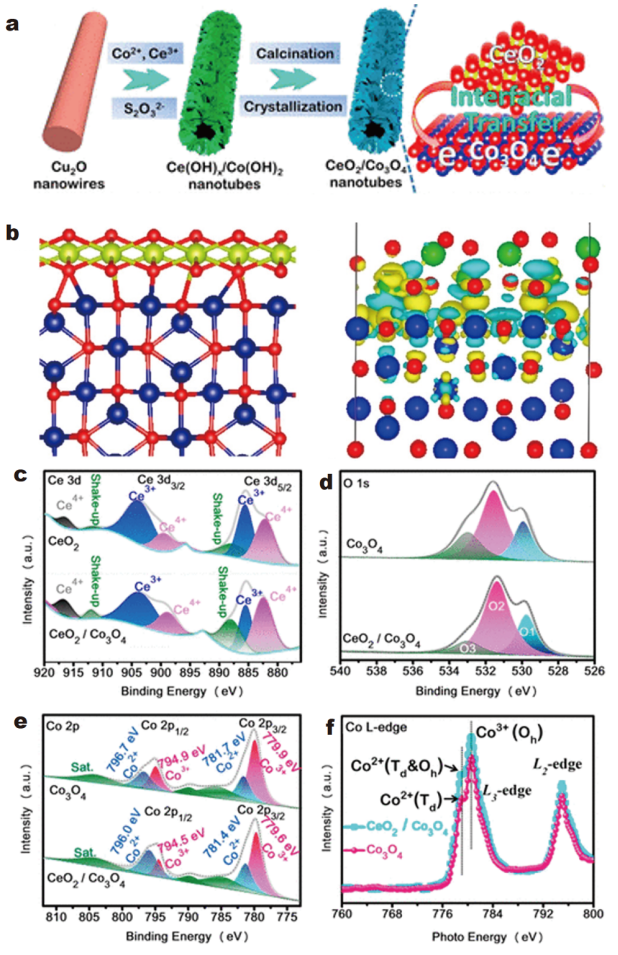

Figure 8 (a) Illustration of the fabrication process of CeO_2/Co_3O_4 hybrid nanostructure; (b) model and charge-density difference of the CeO_2 (111)/Co_3O_4(110) interface; (c) Ce 3d XPS of CeO_2 and CeO_2/Co_3O_4; (d) O 1s and (e) Co 2p XPS spectra of Co_3O_4 and CeO_2/Co_3O_4; (f) Co L-edge X-ray absorption near-edge structure (XANES) of Co_3O_4 and CeO_2/Co_3O_4. Adapted with permission from Ref. [149], Copyright 2019, American Chemical Society.

Substantial OVs are also found in Pt/TiO_2 [151], Pd/CeO_2 [152], Cu/CeO_2 [153], and Ag/MnO_2 [143] at the interface between the pure metal and the oxide matrix. Qu *et al.* [143] found that Ag promoted the formation of OVs in MnO_x. Presumably, Ag^+ species are generated at interface, which enhances the interaction between Ag and Mn species, and more OVs then develop on the Ag-embedded MnO_x. Gac *et al.* [154] demonstrated with temperature-programmed desorption (TPD) and temperature-programmed reduction (TPR) analysis that Ag can increase the oxygen mobility of MnO_x at low temperature to benefit the formation of OVs. By calculating the atomic and electronic structure of the CeO_2 (111) surface in the presence and absence of Pd, Yang *et al.* [152] reported that the E_V at the Pd/CeO_2 (111) interface was about 0.4–0.8 eV lower than at the CeO_2 (111) surface.

Theoretical studies on the formation of OVs

To determine the relationship between the structure and properties of the materials at atomic level, it is indispensable to examine the thermodynamics and kinetics of OVs formation by theoretical analysis [155,156]. It has been generally accepted that the formation of OVs involves of the destruction of the M–O bonds of the metal oxide. Hence, the E_V is normally found to be highly dependent on the M–O bond of the metal oxide. Michalsky *et al.* [157] found by DFT that the E_V on the surface of the metal oxide correlated with the free energy of formation of the bulk metal oxide (i.e., $G_{\text{bulk oxide}}$), and a lower $G_{\text{bulk oxide}}$ corresponded to lower E_V on the surface of the metal oxide. Deml *et al.* [61] also performed DFT calculations of perovskite oxides of different transition metals and found their E_V falling in order of $LaCrO_3$ > $LaFeO_3$ > $LaMnO_3$ > $LaCoO_3$ > $LaNiO_3$ (Fig. 9). In fact, the E_V is closely related to the formation enthalpies of the metal oxide, an indicator of the average M–O bond strength. Hence, it can be expected that the formation of OVs depends greatly on the structure of the metal oxide, including phase, crystal plane, crystallinity, and strain.

Oxides with same chemical component frequently have different phase states. For example, Hara *et al.* [158–161] found phase-dependent E_V of MnO_2 falling in the order of α-MnO_2 > γ-MnO_2 > λ-MnO_2 > β-MnO_2, which was the exact inverse order of their oxidative power (Fig. 10). This is consistent with theory and experiment, where a lower E_V indicates a better oxidant. In a related study, Hayashi *et al.* [158] revealed from DFT calculations how E_V varied for different types of MnO_2 with distinct structure and bearing disparate types of constituent

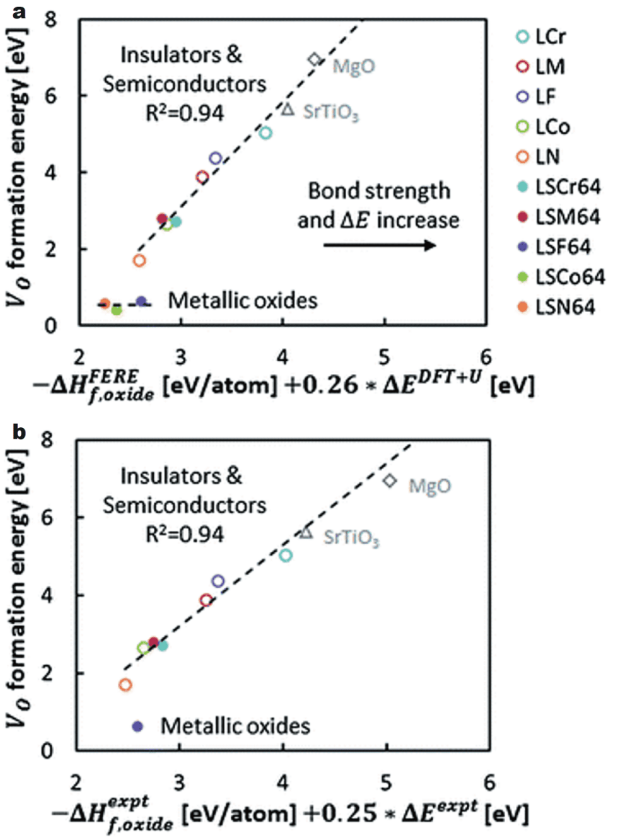

Figure 9 E_V for $LaBO_3$ (LB) and $La_{1-x}Sr_xBO_3$ (LSB) of varying compositions as a function of the linear combination of (a) calculated and (b) experimental band gap energy (ΔE) and formation enthalpy ($\Delta H_{f,\text{ oxide}}$) of the oxide. Adapted with permission from Ref. [61], Copyright 2014, The Royal Society of Chemistry.

oxygen atoms. Specifically, β-MnO_2 consists of planar μ_3-oxygen atoms and thus has a lower E_V (3.25 eV), whereas λ-MnO_2 only has bent μ_3-oxygen atoms and the corresponding E_V is higher (3.44 eV). In sharp contrast, α-MnO_2 and γ-MnO_2 contain both types of oxygen atoms and thus have two E_V values (bent, 3.25 and 3.15 eV; planar, 3.95 and 3.84 eV, respectively). From the structural point of view, E_V is generally lower at the bent oxygen site than at the planar oxygen site. The exception is β-MnO_2, for which the planar oxygen site has a lower E_V.

Crystal planes possess different E_V if they have distinct chemical composition or surface geometry [162–164]. Xie *et al.* [165] demonstrated that compared with the (002) plane, the (111) plane of CeO_2 was more compact and less prone to accommodate OVs. Li *et al.* [162] pointed out that the BiOCl (010) surface can host OVs more easily than the BiOCl (001) surface because the former had an open channel structure. Tompsett *et al.* [166] system-

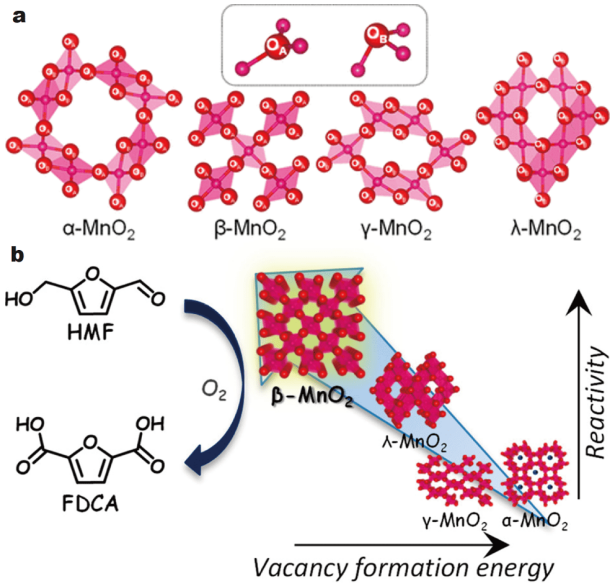

Figure 10 (a) Structural model of different MnO_2 phases; (b) the relationship between reactivity and E_V of different MnO_2 phases. Adapted with permission from Ref. [158], Copyright 2019, American Chemical Society.

atically investigated β-MnO_2 with regard to surface chemistry and catalytic performance. According to DFT calculations, crystal planes with varying degrees of exposure have different E_V [167]. For β-MnO_2, the (311) plane has the lowest E_V of 0.96 eV, and the (001) plane has the highest E_V of 1.43 eV (Table 2). Higher surface energy is more likely to result in higher E_V. In fact, the surface energy is 1.08 eV for the (311) plane and 1.80 eV for the (001) plane. Moreover, OVs are more inclined to form on the surface than in the bulk.

The crystallinity of the material also affects E_V. Amorphous materials are more prone to form defects than long-range ordered crystalline materials. Amorphous metal oxides lack highly ordered arrangement in the three-dimensional (3D) space, and both the metal and the O atoms have weaker lattice constraint and charge localization [168]. In fact, OVs are readily found in amorphous materials, such as SnO_2 [169], CoO_x [170], etc. Duan *et al.* [171] found that amorphous NiFeMo oxide formed abundant OVs after oxygen evolution reaction (OER), but fewer OVs were formed for the crystalline NiFeMo oxide. They speculated that the amorphous NiFeMo oxide possibly allowed more rapid diffusion and reconstruction of metal ions, giving rise to a lower E_V.

Table 2 E_V for different crystal planes of β-MnO_2. Adapted with permission from Ref. [166], Copyright 2014, American Chemical Society.

Miller index	E_V (eV)
(100)	1.13
(101)	1.26
(001)	1.43
(110)	0.98
(211)	1.09
(311)	0.96
Bulk	2.26

Nanostructured materials are appealing precursors of OVs-rich catalysts due to their relatively large surface area and good exposure of coordinated atoms, both facilitating the generation of OVs [172,173]. As an exemplary 2D nanomaterial, ultrathin Bi_2MoO_6 nanosheets show higher OVs concentration and better performance in the photocatalytic degradation of phenol when compared with bulk Bi_2MoO_6 [174]. Similarly, the activity of BiOCl in the degradation of RhB was found to be closely related to the thickness of BiOCl: the thinnest BiOCl nanosheet had the highest amount of OVs and the best catalytic activity [175]. In the case of 1D nanomaterials, Liao *et al.* [176] found that the OVs concentration of ZnO nanorods increased when the diameter was lower. A size-dependent variation of OVs concentration was also found in CeO_2: the OVs concentration in CeO_2 was decreased from 4×10^{20} cm^{-3} (1.7%) to 7.2×10^{18} cm^{-3} (0.028%) as the crystal size increased from 4.6 to 60 nm [177].

It must also be noted that crystal strain (compressive or tensile) also affects OVs formation. Petrie *et al.* [178] calculated the E_V of the $SrCoO_x$ with varying strain and found that the formation of OVs was determined by the compressive strain but aided by the tensile strain, because the tensile strain weakened the Co–O bond and gave a lower E_V (Fig. 11). However, in the case of OVs in thin $SrTiO_3$ films, Iglesias *et al.* [179] concluded that compressive strain reduced E_V and was beneficial for the formation of OVs.

Characteristics of different strategies are summarized in Table 3, availing researchers to choose an appropriate strategy.

CHARACTERIZATIONS OF OVs

Advanced techniques for material characterization are required for elucidating the mechanistic features of OVs in catalytic reactions. Several techniques are suitable for identifying OVs, including XPS, EPR, UV-vis diffuse reflectance spectra (UV-vis DRS), thermal gravimetric analyzer (TG), and temperature-programmed desorption (TPD-MS), X-ray absorption fine structure spectroscopy (XAFS), scanning tunneling microscopy (STM), and DFT

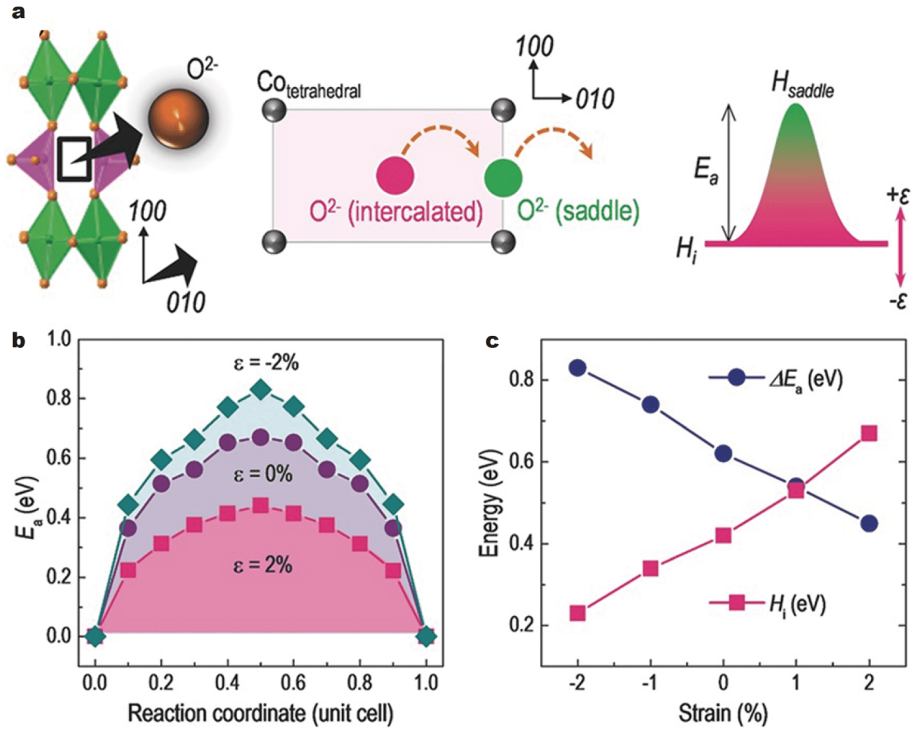

Figure 11 (a) The path and energy barriers (E_a) for oxygen ion movement in brownmillerite phase $SrCoO_x$ through OVs channels when the oxide undergoes a topotactic oxidation to form perovskite phase $SrCoO_3$; (b) as an oxygen ion moves from one intercalation site to another along the [010] direction of the OVs channel, the E_a increases as the strain rate tends from +2% to −2%, where higher E_a is more difficult for OVs to form; (c) a summary of the intercalation enthalpy (H_i) and the activation energy (ΔE_a) as a function of strain. Adapted with permission from Ref. [178], Copyright 2016, WILEY-VCH Verlag GmbH & Co. KGaA, Weinheim.

Table 3 Advantages and shortcomings of developed synthetic strategies for OVs

Synthetic strategy	Temperature	Required atmosphere or reagent	Controllability	Structural damage
High-energy particle bombardment	Ambient	Ar/Xe/He…	Atmosphere Time Pressure	Minimal
Thermal treatment	High	He/N_2/Ar/air/vacuum	Temperature Time Atmosphere Pressure	Slightly
Chemical reduction	Ambient	H_2/NH_3/reducing regents	Reducibility Time	Slightly, but may incurphase transformation
Ion doping	Ambient	Dopants	Type of dopant ion Concentration of dopant ion	Introduce dopant, and may incur phase transformation
Interfacial engineering	Ambient	Not required	Type of noble metal Type of transition metal oxides Heterostructure	New hybrid structure

modeling [180–183].

XPS is a facile method to examine the oxidation state of elements on the surface of metal oxides [184]. It gives the O 1s spectra of oxides, which can frequently be deconvoluted into two or three distinct peaks corresponding to oxygen atoms of distinct states. In general, the peak at 529.3–530.5 eV represents oxygen in the lattice, the peak at 530.5–531.7 eV can be ascribed to the adsorbed oxygen on OVs, and the band at 531.8–532.8 eV corresponds to adsorbed H_2O on the oxide. The relative OVs con-

centration can be estimated by dividing the area of the OVs peak to the area of the whole O 1s or the lattice oxygen peak. Liao *et al.* [176] disclosed that the OVs concentration of ZnO depended on the time when it was treated with H_2 plasma: 57% for 30 s and 76% for 60 s, and that the ZnO rich in OVs gave higher catalytic performance for CO_2 reduction. In addition, XPS also shows the oxidation state of metals in the oxides. Generally, when low valence ions like M^{3+} or M^{2+} exist in MO_2, VOs are created to maintain the electrostatic balance [185–187]. For example, Jiang *et al.* [93] synthesized a series of Co_3O_4 by varying the temperatures at 300, 500, and 700°C. The Co^{2+}/Co^{3+} ratio of the Co_3O_4 falls in the order of 300°C (1.30) > 500°C (1.05) > 700°C (0.78), and the peak area ratio of OVs/whole O 1s falls in the order of 300°C (0.35) > 500°C (0.25) > 700°C (0.18). Therefore, more OVs are generated at lower temperature.

EPR is a common technique to assess unpaired electrons. A characteristic EPR signal around g = 2.004 is related to electron trapping at OVs. Fan *et al.* [188] found that the EPR signal at g = 2.004 had higher intensity for OVs-rich BiOI nanosheets than perfect BiOI. Xie *et al.* [189] proved that Au nanoparticles promoted the formation of OVs on TiO_2 nanorods annealed in H_2. The intensity of the EPR signal at g = 2.004 falls in the order of $Au/TiO_2/H_2$ > TiO_2/H_2 > pristine TiO_2.

UV-vis DRS, TG, and TPD-MS also provide useful clues regarding OVs. For instance, Guo *et al.* [190] doped CeO_2 with rare earth metal, and the resulting material showed enhanced light absorption at 255 nm compared with pure CeO_2 thanks to the presence of OVs. TG can reveal whether OVs are refilled with oxygen, which readily occured at high temperature. For instance, at >260°C, bulk Bi_2MoO_6 displays drastic weight loss but ultrathin Bi_2MoO_6 nanosheets rich in OVs have a much lower weight loss [174]. Zhu *et al.* [191] demonstrated with TPD-MS how the O atom in MnO_2 lattice overflowed to create O_2 and OVs during calcination. Raman spectroscopy provides information related to chemical bonds and structural characteristics. Jin *et al.* [192,193] found that the intensity of characteristic peaks of ZnO at 332, 379 and 437 cm^{-1} weakens in the presence of abundant OVs.

OVs may give rise to a low oxygen coordination number of oxides, and XAFS is a powerful tool to determine the local atomic arrangements of metal oxides. For instance, Zhang *et al.* [194] fitted the WL_3-Edge EXAFS and found that the oxygen coordination number of W was lower in OV-rich WO_3 (5.4) than in commercial WO_3 (6). Zhao *et al.* [60] studied how Cu doping affected the TiO_2 OVs during photocatalytic N_2 fixation. They found from XAFS spectra data a decrease in both the intensity of the Ti–O shell peak and the Ti coordination number in TiO_2 when the amount of Cu dopant escalated from 0% to 6%. After further calculation, the OVs concentration of 0%, 1%, 3%, and 6% Cu-doping TiO_2 was found to be 0.985%, 1.845%, 2.195% and 8.621%, respectively. Tan *et al.* [195] also inferred from the XAFS result of NiAl-LDH with different thickness that the OVs concentration of monolayer and few layers NiAl-LDH was 1.80 and 2.14 nm^{-3}, respectively.

STM images reveal the local atomic arrangement of the oxide surface and hence show in a very straightforward manner of the absence of O atoms in lattice. Feng *et al.* [196] used STM to simulate the electrocatalytic hydrogen evolution reaction (HER) process and found that OVs acted as active sites to absorb and dissociate water during catalysis. In monitoring the CO oxidation on Au/CuO surface, Zhou *et al.* [104] found dark features in the STM image of the Au/CuO surface that corresponded to the presence of OVs due to the release of lattice oxygen. These OVs disappear after Au/CuO is treated at 400 K in O_2. Esch *et al.* [197] applied STM to measure the OVs concentration in CeO_2 and suggested that the concentration of surface and subsurface OVs was 1.5% and 1.3% of the surface atoms, respectively.

DFT is a powerful method that constructs theoretical models at atomic and molecular level to analyze changes in electronic structure and assess catalytic mechanism of materials bearing OVs. DFT calculations help estimate bandgap changes [198], charge separation [55], as well as adsorption and activation of substance involving in catalytic reactions [199,200]. The energy barrier for the rate limiting step of a catalytic reaction can also be calculated to evaluate how OVs impact the efficiency and selectivity of the catalysis [198]. Zhang *et al.* [198] demonstrated with DFT calculation that OVs narrowed the bandgap of CeO_2 and can enhance optical absorption to facilitate photocatalytic water oxidation. Huo *et al.* [55] found that OVs on the Bi_2WO_6 surface had lower adsorption energy for O_2, and the O–O bond length of O_2 adsorbed at OVs was longer than at the perfect surface. The findings correspond to efficient photocatalytic NO oxidation by O_2 on the OVs surface.

MATERIAL PROPERTIES OF METAL OXIDES THAT ARE ADJUSTED BY MANIPULATING OVs

Current photocatalysts often suffer from low photoconversion efficiency and catalytic selectivity because of

their limited light absorption capacity, inadequate reaction kinetics, undesirable electron conductivity, etc., and thus fail to meet the demands of practical applications [201–204]. The OVs in metal oxides play a key role in the mechanism and kinetics of the redox reactions mediated by the metal oxides [149], and have been employed to tune the catalytic performance of TiO_2 [1,7,205], CeO_2 [206], ZnO [7,85,207,208], CuO [12,13,209]. In fact, tuning OVs can help improve multiple aspects of the photocatalytic process simultaneously, including light absorption [44,50], charge transfer and separation [49,210], and surface reaction [211,212]. Similarly, regulating OVs to improve catalytic activity is also commonly used in electrocatalysis and thermal catalysis [213–216]. Understanding the principles of action hence not only helps understand how OVs affect the material properties but also guides the design of catalysts with high activity and selectivity. In this section, we approach the effects of OVs on the material properties of the photocatalyst from several aspects, including examples from electrocatalysis and thermal catalysis.

Band structure

Effective capture of solar irradiation is essential for semiconductor photocatalysts, yet oxide-based photocatalysts normally have a wide band gap (>3.0 eV) that can only respond to UV light (<315 nm). Regulating the band structure of photocatalysts to improve their ability to harvest solar energy has been a challenge. Substantial evidence has been reported over the past decades on how OVs improve the ability of photocatalysts to absorb visible light [217] (e.g., CeO_2 [218], ZrO_2 [219,220], Ga_2O_3 [221], BiOBr [222], BiOCl [223], $BiVO_4$ [55], $BiFeO_3$ [224], $BiPO_4$ [224], Bi_2WO_6 [223], TiO_2 [148,105]). New defect levels created by OVs render either a downshift of the conduction band (CB) minimum or an upshift of the valence band (VB) maximum, and the narrowed band gap then allows electron excitation by visible light [64,225] or even NIR irradiation [124].

The VB maximum tail is extended when the new defect level that originates from OVs overlaps with the VB maximum [107,123,226–228]. In studying hydrogenated TiO_2 (H_2-500) [226], Lv *et al.* [107] found that the OVs-rich TiO_2 absorbed visible light and estimated a slightly upward shift of the VB maximum edge from the UV-vis DRS and XPS VB spectra (Fig. 12a–c). Lv *et al.* demonstrated an improved absorbance of OVs-rich $BiPO_{4-x}$ in 300–800 nm due to the broadened VB. Geng *et al.* [227] performed DFT calculations to describe how OVs tuned the band gap of the ZnO slab (Fig. 12d, e). A new defect level appears near the VB maximum of the OVs-rich ZnO slab, and electrons tend to accumulate around the defect energy level, which reduces the transition energy of excited electrons. Except for the effect on the VB, OVs may also form a donor level or localized electron states near the CB. Ansari *et al.* [228] gave conclusions different to those of Zeng in studying ZnO (Fig. 12f, g). They prepared ZnO with OVs (m-ZnO), whose CB overlaped with the defect level of OVs and was lowered distinctly. In fact, the defect level of OVs may also form between the VB and CB as an intermediate level, as is the case in OVs-$BiVO_4$, in which Feng *et al.* [229] revealed from DFT an interband state between VB and CB (Fig. 12h).

Upon visible light irradiation, the defect level can accept electrons excited from the VB [19], and electrons in the defect level also can be excited to the CB [230]. Lei *et al.* [231] disclosed the presence of a defect level in the band gap of oxygen-deficient In_2O_3, where electrons can not only enter the defect level from the VB but also be further excited from the defect level to the CB. All these processes allow excitation of electrons by visible light. Similarly, Wang *et al.* [230] proved the existence of an intermediate level between the CB and VB of OVs-rich BiOCl and demonstrated the electron transition from VB to CB *via* the intermediate level under visible light irradiation (Fig. 12i). Yu *et al.* [232] modulated the concentration of OVs in $Sr_2Bi_2Nb_2TiO_{12}$ nanosheets (SBNT-HR) for the fine and continuous control of the band gap from 3.28 to 2.41, 2.28, and 2.11 eV, respectively (Fig. 13). After creation of OVs, the photoresponse of $Sr_2Bi_2Nb_2TiO_{12}$ is extended from the UV to the visible region, and its CO_2 photoreduction activity increases to about 58 times that of its bulk.

Transfer of electrons

Electron transfer is generally considered as a critical step in the catalytic reaction of CO_2. Hence, it is indispensable to develop approaches to engineer the electronic properties of catalysts, for which OVs provide a facile strategy. The critical roles of OVs in promoting charge transfer have been well documented [233–237]. It has been shown that OVs can inhibit the recombination of photogenic electron-holes because photo-induced conduction electrons preferentially enter OVs rather than recombining with holes [227,238]. For example, Sun *et al.* [239] demonstrated the high efficiency of OVs-enriched $BiOIO_3$ in removing Hg^0 and proposed, based on XPS and FT-IR characterizations, that the OVs acted as positive charge centers to trap electrons and thus inhibited the recombination of photo electron-hole pairs. Magyari-Köpe

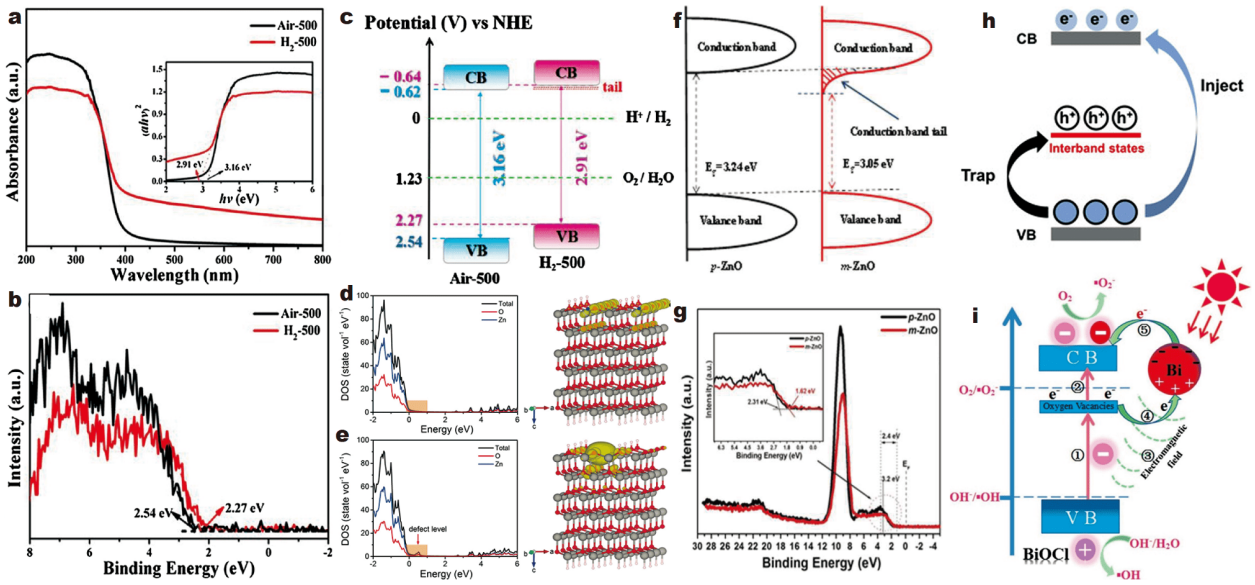

Figure 12 (a) UV-vis DRS of TiO_2 treated by air (Air-500) and H_2 (H_2-500) to determine the optical band gaps, with the corresponding Tauc plots in the inset; (b) XPS valence band spectra and (c) energy band diagrams of the Air-500 and H_2-500 TiO_2. Adapted with permission from Ref. [226], Copyright 2018, Elsevier; calculated density of states (DOS) and partial charge density around the VB of (d) ZnO and (e) ZnO with an OV (gray, Zn; red, O; white, H atoms; yellow regions, charge density contour). Adapted with permission from Ref. [227], Copyright 2018, Wiley-VCH Verlag GmbH & Co. KGaA, Weinheim; (f) the density of electronic states for OVs-free ZnO (p-ZnO) and m-ZnO; (g) XPS valence band spectra of p-ZnO and m-ZnO; the inset shows the zoomed valence band spectra. Adapted with permission from Ref. [228], Copyright 2013, The Royal Society of Chemistry; (h) the OVs induce n-type doping mechanism under illumination. Adapted with permission from Ref. [229], Copyright 2019, Wiley-VCH Verlag GmbH & Co. KGaA, Weinheim; (i) mechanism of plasmonic photocatalysis on Bi/BiOCl. Adapted with permission from Ref. [230], Copyright 2017, Elsevier.

et al. [240] also found that an OVs-rich filament induced several defect states within the band gap of TiO_2, which subsequently led to defect-assisted electron transport.

In addition, accumulation of electrons around the VB maximum or CB minimum often promotes charge separation as well. From DFT calculations, Geng *et al.* [227] found that the presence of OVs increased the charge density of ZnO around the VB maximum, which enhanced the activation of CO_2. In addition, OVs are also electron donors that improve the electronic conductivity of the catalyst [109,241]. For instance, thanks to the presence of the OVs, the electron transport layer of OVs-rich TiO_2 possesses high electron density and electrical conductivity [242]. This phenomenon is not restricted to TiO_2 but found in many other metal oxides as well, including VO_2 [243], Sr_2FeMoO_6 [244], TiO_2 [72,245], Cu_2O [246], $BiOIO_3$ [239], $BaCeO_3$ [247], BiOCl [248,249], α-Fe_2O_3 [250], etc.

It must be noted that excessive OVs may end up trapping electrons and restraining electron mobility [251], which is probably why catalyst with abundant OVs sometimes gives weak photocurrent density and low catalytic performance compared with catalyst with fewer OVs. From the molecular orbital (MO) theory and Cambridge Sequential Total Energy Package (CASTEP) method, Gan *et al.* [251] suggested that excessive OVs on the In_2O_3 can form an impurity band with unlocalized MO to trap electrons excited from VB to CB (Fig. 14a–c). Indeed, the incident photon-to-current efficiency (IPCE) is only 35% for In_2O_3 when there is an excessive amount of OVs but reaches 70% when the amount of OVs is kept moderate. Li *et al.* [252] also obtained a similar conclusion in calculating the electronic structure of β-MnO_2 with DFT+*U* and showed that excessive OVs began to weaken the charge density on the (110) crystal plane (Fig. 14d,e).

Adsorption and activation of molecules

The adsorption and activation of substrate molecules can also be enhanced by preparing OVs-rich catalysts and introducing oxygen-deficient and electron-rich surface states [248,253–258]. Upon contact, the OVs-rich catalyst changes the state of the reactant (e.g., bond length, bond angle, coordination mode or intermediates) [259–264]. The deficiency of oxygen in the lattice increases the amount of uncoordinated active sites, and thus improves

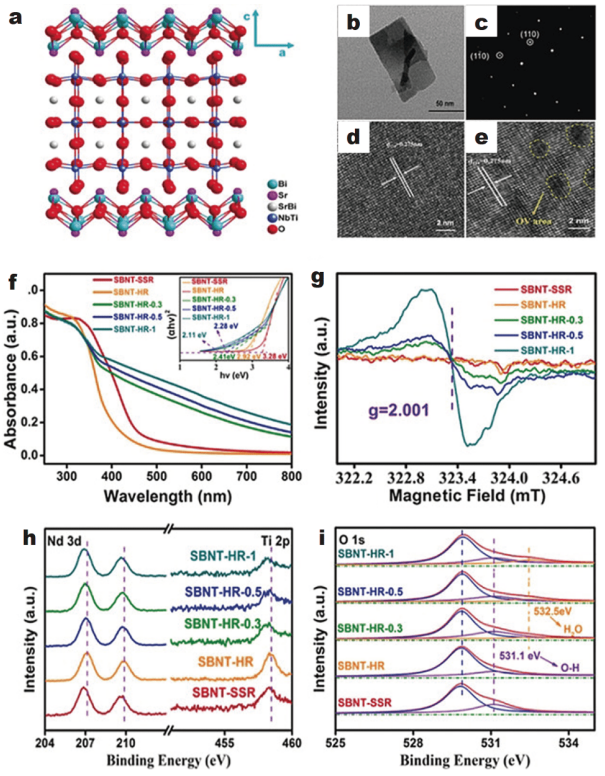

Figure 13 (a) Crystal structure of $Sr_2Bi_2Nb_2TiO_{12}$ nanosheets (SBNT-HR) without OVs; (b) TEM image and (c) SAED pattern of SBNT-HR-0.5 (SBNT-HR treated with 0.5 mL glyoxal to create OVs); (d) HRTEM image of SBNT-HR; (e) HRTEM image of SBNT-HR-0.5; the OVs concentration of the bulk (SBNT-SSR), the perfect nanosheets (SBNT-HR), and the defective nanosheets (SBNT-HR-*X*, *X* denoting the amount of glyoxal used to treat SBNT-HR to create OVs, *X* = 0.3, 0.5, and 1 mL) are determined by (f) UV-vis DRS (band gap shown in inset), (g) EPR, (h) Nd 3d, Ti 2p, and (i) O 1s XPS. Adapted with permission from Ref. [232], Copyright 2019, Wiley-VCH Verlag GmbH & Co. KGaA, Weinheim.

the affinity of the oxides toward ions or molecules. For instance, Zhang *et al.* [211] reported extremely high adsorption affinities of OVs-rich WO_x/C nanowire toward Pb^{2+} (1224.7 mg g^{-1}) and methylene blue (1188.3 mg g^{-1}). Similarly, OVs confined in ultrathin $NiCo_2O_4$ nanosheets lower the energy barrier for the adsorption of H_2O and improve the OER efficiency [39].

With regard to the reactant, the OVs as electron capture sites can modulate both the coordination structure and the electronic states of the adsorbed reactant, thereby facilitating the activation of molecules [116,232,258,265–271]. For instance, Li *et al.* [248] showed in the case of Au-supported OVs-rich BiOCl, the OVs on BiOCl can facilitate the trapping and transfer of plasmonic hot electrons to the adsorbed O_2 to produce $\cdot O_2^-$. Tan *et al.* [272] performed a scanning tunneling microcopy (STM) study on the adsorption and dissociation of molecular O_2 both at the bridge-bonded OVs (BBOVs) and at the hydroxyls (OH^-) on the TiO_2 (110) surface. Whereas the singly adsorbed molecular O_2 at BBOVs is activated and can be dissociated *via* an intermediate state driven by the STM tip, the singly adsorbed molecular O_2 at the hydroxyls survives the tip-induced effect. Zhang *et al.* [273] designed OVs-abundant InO_x and verified that the OVs improved the catalytic activity of InO_x in CO_2 electroreduction by changing the coordination environment of CO_2. In the temperature-programmed desorption of CO_2 (CO_2-TPD), OVs-abundant InO_x has two different temperatures for the chemical desorption of CO_2 (389.3 and 413.9°C), but OVs-poor InO_x has only one (364.7°C), indicating that OVs improve the chemisorption ability and capacity of InO_x for CO_2.

Theoretical calculations help describe the relevant structural changes of substrates at the molecular and atomic level. In general, OVs activate reactants by weakening the chemical bond or changing the bond angle. Yu *et al.* [232,267] found that OVs-rich $Sr_2Bi_2Nb_2TiO_{12}$ required a much lower adsorption energy (−0.377 eV) and a smaller O–C–O bond angle (126.0°) for the adsorption of CO_2 than the stoichiometric $Sr_2Bi_2Nb_2TiO_{12}$ (−0.125 eV and 179.0°). Huygh *et al.* [274] investigated the adsorption, dissociation, and diffusion of CO_2 on the (001) surface of anatase (TiO_2) with DFT calculations (Fig. 15). A new highly stable adsorption configuration of CO_2, residing one of the O atoms of CO_2 inside the OVs, was proposed with the introduction of OVs, leading to a stronger activation of C–O bond and a possible exothermic dissociation of CO_2. Such a configuration decreases the barrier of the CO_2 dissociation reaction from >45 to 22.2 kcal mol^{-1}. Werner *et al.* [117] examined how OVs within CeO_2 facilitated the selective hydrogenation that converted alkynes to alkenes. The interaction between H_2 and CeO_2, a crucial aspect of the hydrogenation reaction, depends strongly on OVs. According to nuclear reaction analysis (NRA) and DFT calculations, hydrogen species remain as hydroxyls on the surface of stoichiometric CeO_2 but get incorporated into the interior of OVs-rich CeO_{2-x} in the form of hydride species. In fact, enhanced adsorption and molecular activation commonly occur simultaneously in N_2 fixation, CO_2 reduction, and H_2O splitting in the presence of OVs.

The industrial Haber–Bosch process for N_2 fixation to produce NH_3 requires hash conditions (15–25 MPa, 300–550°C), and N_2 fixation under mild conditions remains to be conquered in industry [265]. Prior studies have demonstrated efficient electron transfer from OVs

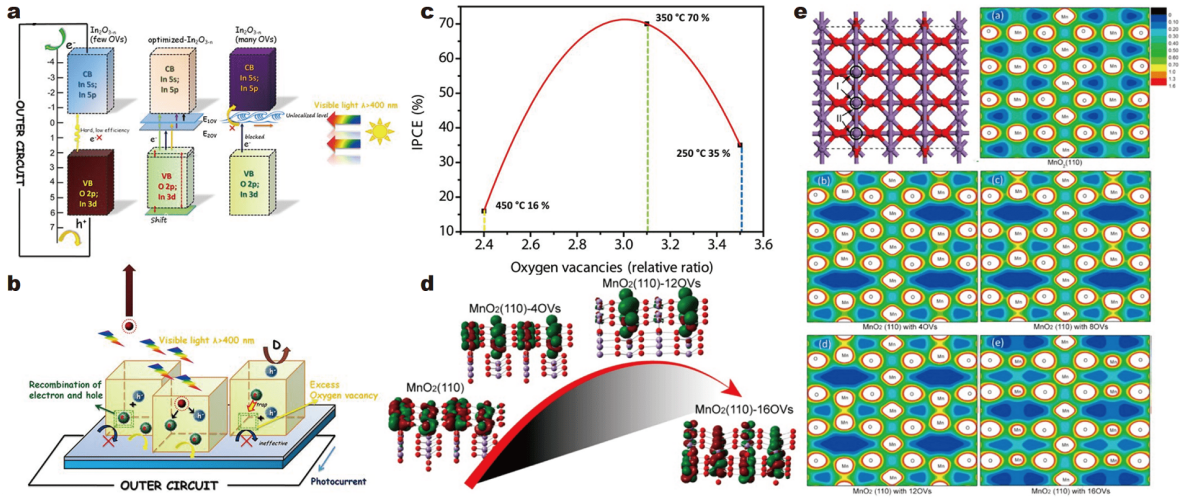

Figure 14 (a) Energy diagram of In_2O_{3-n} with different amounts of OVs; (b) schematic illustration of how excess OVs affect the transfer of photoelectron in photon-to-electron conversion processes; (c) plot of the best IPCE efficiency with visible light (>400 nm) of In_2O_3 obtained by calcination in air at 250, 350, 450°C, as a function of the relative OV amount. Adapted with permission from Ref. [251], Copyright 2013, American Association for the Advancement of Science (AAAS); (d) the charge density of MnO_2(110) varying with the number of OVs; (e) structural model and total charge density of β-MnO_2 (110) with 0, 4, 8, 12, and 16 OVs, respectively. Adapted with permission from Ref. [252], Copyright 2015, American Chemical Society.

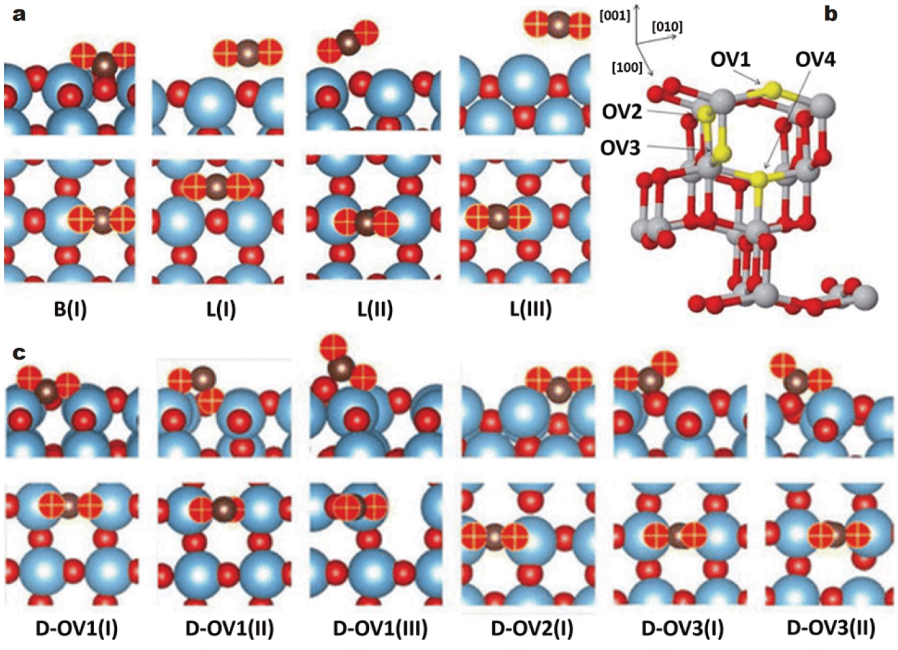

Figure 15 Different adsorption configurations of CO_2 on the anatase (001) surface (a) without and (c) with different OVs, in side view and top view (upper and lower panels, respectively). Ti = blue, O_{TiO_2} = red, O_{CO_2} = red with yellow plus sign, C = brown. B(I) is a strong chemisorbed monodentate carbonate configuration, and L(I), L(II), and L(III) are physisorbed configurations; (b) different OVs on an anatase (001) TiO_2 surface (Ti = gray, O = red, OV = yellow.). Adapted with permission from Ref. [274], Copyright 2016, American Chemical Society.

to N_2, which may promote N_2 adsorption and activate the N≡N triple bond [265,275,276]. Zhang *et al.* [212] also showed how the OVs in atomic layered MoO_2 expedited the chemical adsorption of N_2 on defective Mo sites *via* electron donation. Energy change calculations reveal that in the presence of OVs on MoO_2, N_2 has a low adsorption

energy of −1.05 eV and is much more easily adsorbed. In contrast, the adsorption energy for N_2 on OV-free MoO_2 reaches as high as 1.50 eV. Hence, the OVs-MoO_2 catalyst exhibits high activity and selectivity in N_2 fixation. Li *et al.* [265] further demonstrated the efficient fixation of N_2 to give NH_3 using visible light illumination and BiOBr nanosheets with OVs. Notably, the reaction proceeds without any organic scavenger or precious metal cocatalyst, because the OVs activate the adsorption of N_2 and increase its bond length to 1.133 Å with the interfacial electrons transferred from the excited BiOBr nanosheets. Han *et al.* [277] accomplished the electrochemical synthesis of NH_3 over TiO_2 with abundant OVs. The OVs simultaneously enhance N_2 adsorption and activate the N≡N triple bond, thus promoting the nitrogen reduction reaction (NRR) (Fig. 16). They used DFT studies to reveal that the surface OVs stabilized *NNH, a highly unstable and potentially rate-determining intermediate, hence dramatically lowering the ΔG_{PDS} of the NRR by 1.4–1.7 eV. Without doubt, novel catalysts that exploit the benefits of OVs create unprecedented opportunities to fix atmospheric N_2 through less energy-demanding photo- or electro-chemical processes.

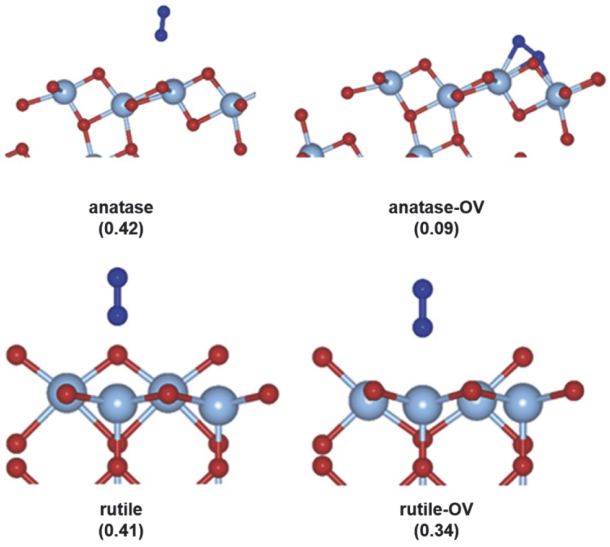

Figure 16 The optimized geometries (side view) and free energy changes (in eV) of $*N_2$ on pristine and OV-containing TiO_2. Cyan, red, and blue spheres indicate Ti, O, and N atoms, respectively. Adapted with permission from Ref. [277], Copyright 2019, Elsevier.

Converting CO_2 to value-added chemicals offers a sustainable solution for carbon cycling and is of significance in solving environmental problems and energy crisis [278,279]. Yang *et al.* [267] found in their systematic theoretical calculations of the absorption and activation of CO_2 on OVs-rich Bi_2MoO_6 (Fig. 17) that the OVs can decrease the adsorption energy of CO_2 and that the localized electrons around the OVs tended to be injected into CO_2 after the adsorption of CO_2, thus facilitating the further hydrogenation of the intermediate *CO to form CH_4. Geng *et al.* [227] developed an efficient strategy to facilitate CO_2 reduction by introducing OVs into electrocatalysts, and mechanistically demonstrated that the OVs improved CO production by increasing the binding strength of CO_2 and reducing the barrier of CO_2 activation.

The photocatalytic splitting of water to generate hydrogen helps combat the energy crisis and environmental problems caused by the overuse of fossil fuels and is a desirable means to access renewable energy. Li *et al.* [280] demonstrated that the adsorption and activation degree of H_2O were different on different surfaces of BiOCl with OVs: H_2O was dissociatively adsorbed on the OVs of the (010) surface but molecularly absorbed on the OVs of the (001) surface (Fig. 18). *In situ* water contact angle measurement clearly shows different states of H_2O molecules on the (010) and (001) surfaces, and verifies that the (001) surface is more hydrophilic. According to DFT results, OVs help cleave the O–H bond on the BiOCl (010) sur-

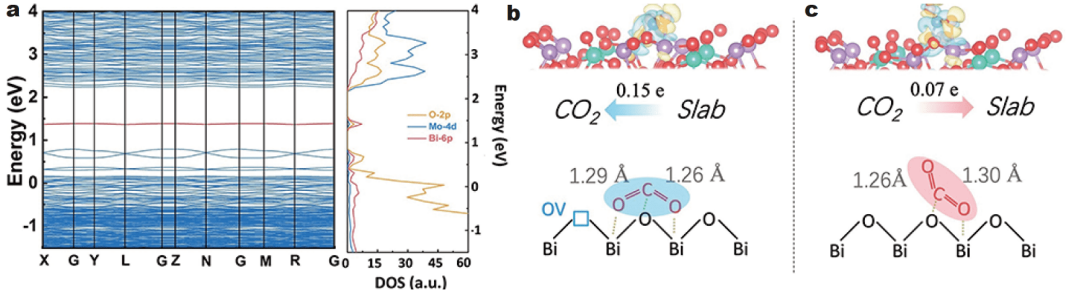

Figure 17 (a) Calculated band structures and DOS of Bi_2MoO_6-OVs, and adsorption of CO_2 on (b) OVs-rich and (c) OV-free Bi_2MoO_6. The yellow and blue iso-surfaces represent the charge accumulation and depletion in the space. Adapted with permission from Ref. [267], Copyright 2019, Elsevier.

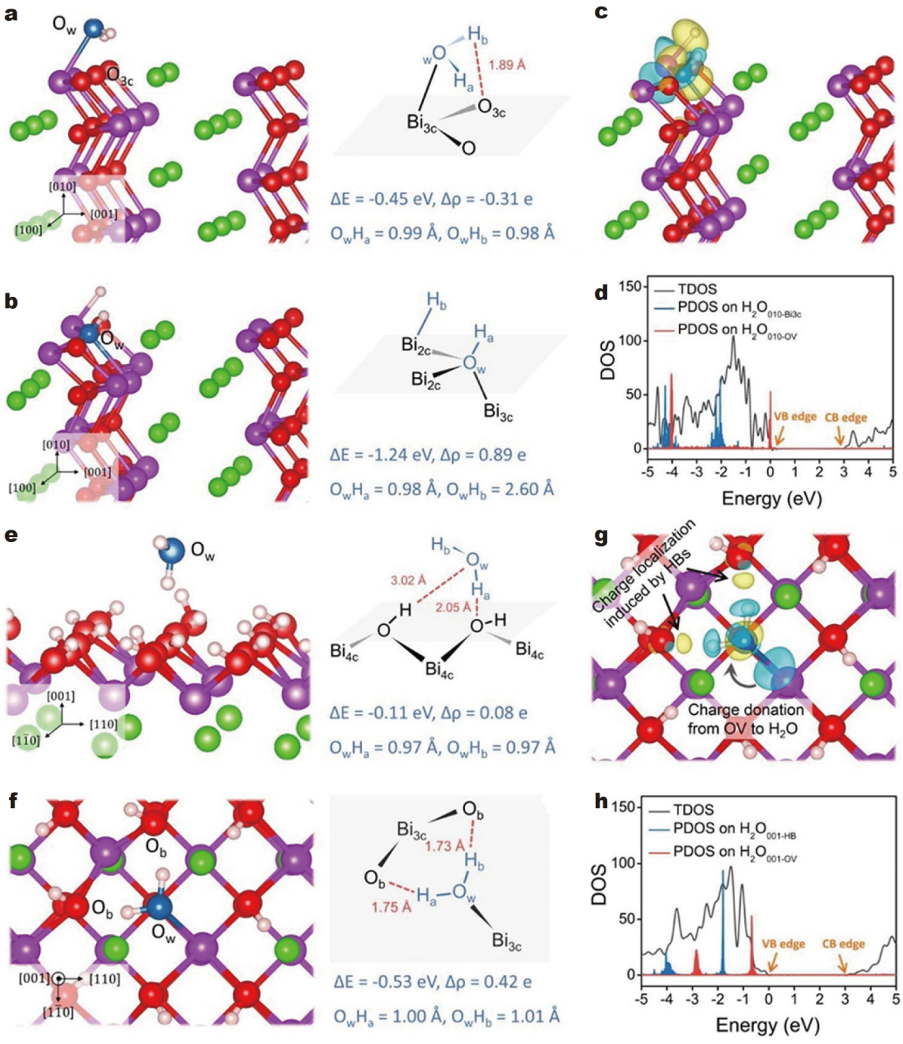

Figure 18 Theoretical study of water adsorption on the defect-free BiOCl (a) (100) and (e) (010) surfaces; theoretical study of water adsorption on the BiOCl (b) (100) and (f) (010) surfaces with an OV; the corresponding charge density difference is given in (c) and (g) for the BiOCl (100) and (010) surfaces respectively; PDOS of H_2O on the (d) (100) and (h) (010) surface of BiOCl with different adsorption structures (HBs: hydrogen bond; ΔE: the water adsorption energy; $\Delta\rho$: the Bader charge change of the adsorbed water). Adapted with permission from Ref. [280], Copyright 2016, American Chemical Society.

face but hinders the cleavage on the (001) surface.

Catalytic oxygen reduction reaction (ORR) is crucial to many energy conversion processes ranging from the sustainable production of hydrogen peroxide (H_2O_2) to fuel cell applications [281]. In case of $LaMnO_3$ and $La_xSr_{1-x}MnO_3$, Staykov *et al.* [281] reported that OVs allowed easier charge transfer from the catalyst surface to the adsorbates and thus accelerated the O_2 reduction kinetics. However, thorough theoretical understanding is still lacking regarding the impact of OVs on the generation of active oxygen and the catalytic cycle of ORR, which limits the rational design of point defect catalysts. Yang *et al.* [116] revealed that OVs promoted O_2 activation on the surface of perovskite oxide for low-temperature CO oxidation. Specifically, they found that O_2 was more favorably adsorbed and activated on surfaces with OVs *via* a one-electron transfer process to form O^-, thus increasing the richness of active O^- to promote the low-temperature oxidation of CO.

Catalysis kinetics

Catalytic reactions that may generate various products at the same time require further separation and purification, thus creating extra trouble to industrial application.

Needless to say, developing catalysts with excellent selectivity to give the desired product specifically is crucial for synthetic applications, but this remains a challenge. Prior studies have demonstrated in a number of cases how OVs advance the selectivity of catalytic reactions [117,282–285]. For instance, whereas commercial noble metal-based catalysts suffer from poor ability to transform NO_x to N_2 [212,286], OVs-rich Pt/CeO_2 and Rh/CeO_2 afford high selectivity in the catalytic conversion of NO to N_2 [287].

Generally, for a catalytic reaction that may lead to multiple products, the reaction pathway with smallest energy barrier is taken among multiple alternatives. It is thus not surprising to see that OVs promote the catalytic selectivity, since they always affect the potential energy barriers of catalytic reactions. For instance, Zhang *et al.* [212] disclosed that OVs-MoO_2 had a high selectivity toward the reduction of N_2 (NRR), as OVs can, *via* the distal/alternating hybrid path, selectively stabilize N_2H^* to form NNH_2^* and then facilitate a direct protonation of NNH_2^* to $HN_2H_2^*$ (Fig. 19). The activation energy of the rate-limiting step is thus reduced to 0.36 from 1.49 eV as is in the case of perfect MoO_2.

Activating CO_2 by OVs impressively shows how OVs affect the selectivity in a complicated catalytic reaction. Two possible pathways have been proposed for CO_2 reduction over TiO_2 surface, i.e., the fast-hydrogenation (FH) pathway and the fast-deoxygenation (FdO) pathway. In a mechanistic study, Ji *et al.* [261] carried out first-principles calculations to examine the pathways of CO_2 reduction on perfect and defective anatase TiO_2 (101) surfaces. Because of unfavorable energy barrier, the FdO pathway can proceed on neither the perfect surface nor the defective surface. In contrast, the defective surface has a much lower barrier for the deoxygenation process in the FH pathway. In the presence of OVs, the catalytic reaction needs fewer protons to promote the formation of CH_4 from CO, because the O in CO does not need two extra protons to form H_2O but will simply stay in the OVs. Yang *et al.* [267] demonstrated with DFT and CO_2-TPD spectra that the hydrogenation of *CHO to CH_4 was more thermodynamically favorable on OVs-rich Bi_2MoO_6 than on perfect Bi_2MoO_6. With the charge density difference introduced by OVs, electrons will be injected into adsorbed CO_2, increasing the C–O bond length from 1.18 to 1.26 or 1.29 Å. In the electrocatalytic reduction of CO_2 to formate [288], OVs-rich Co_3O_4 has a lower onset potential of about 0.78 V and a Tafel slope of 37 mV dec^{-1}, whereas perfect Co_3O_4 has an onset potential of 0.81 V and a Tafel slope of 48 mV dec^{-1}. According to DFT calculations, OVs reduce the energy barrier of the rate-limiting step from 0.51 to 0.40 eV by stabilizing the $HCOO^{-}$* intermediate (Fig. 20).

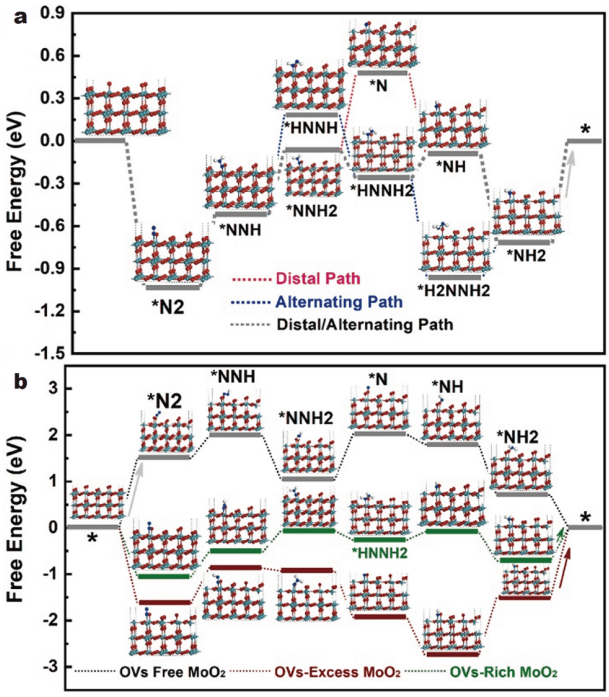

Figure 19 (a) The free energy diagram for different NRR pathways on OVs-rich MoO_2. In the distal pathway (blue dash line), the protonation of NNH* to HNNH* has an energy barrier of ΔG = 0.69 eV, and deprotonation of N_2H_2* to form N* species has ΔG = 0.54 eV. However, the energy barrier is effectively decreased in the distal/alternative hybrid path to ΔG = 0.36 eV; (b) energy profiles for electrocatalytic N_2 reduction on the surfaces of MoO_2 with no OV, rich OVs, and excessive OVs. Adapted with permission from Ref. [212], Copyright 2019, Elsevier.

The synthesis of value-added products having two or more carbons (e.g., gasoline) directly from CO_2 is far more challenging than the hydrogenation of CO_2 to give C1 chemicals, because of the inertness of CO_2 as well as the high C–C coupling barrier. Gao *et al.* [289] developed a bifunctional catalyst consisting of reducible indium oxide (In_2O_3) and zeolites that has high selectivity for gasoline-range hydrocarbons (78.6%) with very low methane selectivity (1%). The OVs on In_2O_3 surfaces activate both CO_2 and H_2 to form methanol, and C–C coupling occurs subsequently inside the zeolite pores to produce gasoline-range hydrocarbons with a high octane number.

Multicomponent catalytic platforms

The integration of multiple functional units of catalysis into complex architecture has sparked rising interest for engineering sophisticated nanomaterials [290–292]. In-

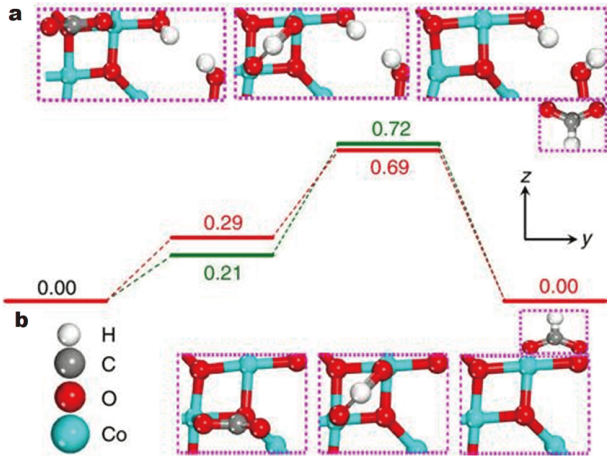

Figure 20 Calculated free energy (in eV) diagrams for the electrochemical reduction of CO_2 to formate on (a) Co_3O_4 with OVs and (b) intact Co_3O_4 single unit cell layers. The first step is an electron transfer to form $CO_2^{\bullet-}$ and the second step involves a simultaneous proton/electron transfer, the product of which gives formic acid. Asterisk denotes the active site. The spheres in white, red, grey, and light blue represent H, O, C, and Co atoms, respectively. Adapted with permission from Ref. [288], Copyright 2017, Nature Publishing Group.

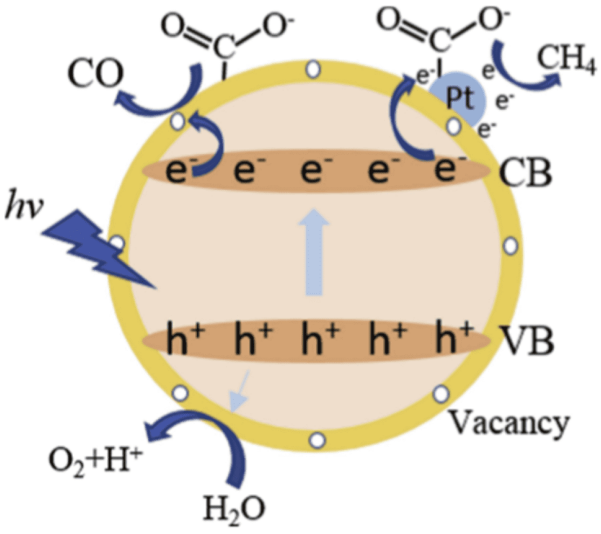

Figure 21 Mechanisms for the photoreduction of CO_2 with H_2O vapor over highly dispersed Pt nanoparticles on ultrathin TiO_2 support Adapted with permission from ref. [295], Copyright 2018, Elsevier.

deed, OVs also engage in multicomponent catalytic platforms to endow reactions with new catalytic mechanisms [293,294].

Recently, atomically dispersed catalysts have attracted tremendous attention for their unique structures and maximized atom utilization. Utilizing noble metals in ultra-small forms (ultrafine nanoparticles, clusters, single atoms) is an effective strategy to increase their usage efficiency and catalytic activity. Liu *et al.* [295] demonstrated that OVs-rich ultrathin TiO_2 decorated with highly dispersed Pt nanoparticles exhibited excellent photocatalytic activity for the conversion of CO_2 to CH_4 and CO with a total electronic yield of 666.6 μmol g^{-1} h^{-1}. Electron transfer from the OVs-rich ultrathin TiO_2 to Pt results in a faster separation of photogenerated electrons-holes, and the OVs also enable stronger adsorption of CO_2 (Fig. 21).

Chen *et al.* [296] found that in the CO_2 reduction over single Cu atom on OVs-rich TiO_2, the dissociation of CO_2 preferentially occured at the Cu/OV/TiO_2 interface. The combination of Cu atoms with OVs-rich TiO_2 facilitates the adsorption of activated bent CO_2 as well as CO_2 dissociation. Specifically, the adsorption intensity of bent CO_2 ranks in the order of Cu/OV/TiO_2 > OV/TiO_2 > Cu/TiO_2 > TiO_2 (Fig. 22). The as-formed Cu/OV complex can lower the reaction barrier for CO_2 dissociation (CO_2* → CO* + O*) to a very low level (0.10–0.19 eV) to expedite the production of CO.

The study on Cu/CeO_{2-x} also highlights how multi-

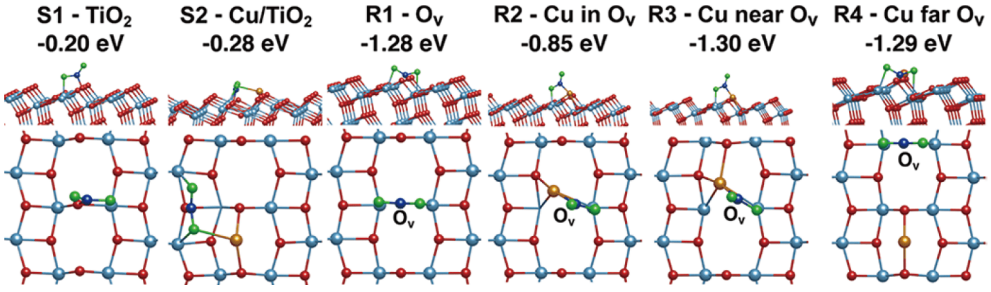

Figure 22 Most stable adsorption geometries and adsorption energies of bent CO_2 on (S1) a stoichiometric TiO_2 surface, (S2) a stoichiometric TiO_2 surface with a Cu atom, (R1) a reduced TiO_2 surface with OV, (R2) a reduced TiO_2 surface with a Cu atom in an OV, (R3) a reduced TiO_2 surface with Cu near an OV, and (R4) a reduced TiO_2 surface with Cu far from OV. Adapted with permission from Ref. [296], Copyright 2018, American Chemical Society.

component catalytic platforms can aid the discovery of new mechanisms to promote CO_2 reduction. Varandili *et al.* [259] demonstrated how the unique active sites at the Cu/CeO_{2-x} interface stabilized CO_2 intermediates with a bidentate adsorption involving both CeO_{2-x} OV sites and Cu, which promoted the activity of CO_2, improved the selectivity for generating methane, and allowed reaction engineering beyond the limits of scaling relationship (Fig. 23).

Synergy may also occur between two different types of defects. Some cationic defects also exist in some oxygen-deficient materials. Wu *et al.* [297] built a new homojunction of TiO_2 and proved both experimentally and with DFT that the oxygen and titanium vacancies changed the charge density of the resulting TiO_2, and demonstrated the performance of the homojunction in photocurrent generation, photocatalysis, and energy storage (Fig. 24).

CHALLENGES AND PERSPECTIVES

Engineering OVs-mediated catalysis requires a thorough understanding of OVs regarding both their formation and their modes of action. Atomic level details on the interactions between metal oxides and defects need further elucidation, because understanding these various features will shed light on rational catalyst design. However, to date, many aspects of OVs still remain significant scientific challenges and call for exploration.

Manipulating OVs, the prerequisite to elucidating mechanistic features in catalytic activity, remains a daunting challenge. To date, it remains difficult to attain fine control over the concentration and spatial location of OVs in a given catalyst while maintaining the structural integrity of the catalyst precursor. First of all, it must be noted that the contribution of OVs depends highly on their concentration. Excessive OVs trap electrons and restrain electronic mobility, which explains why catalysts with an unduly high amount of OVs have poorer photocatalytic performance than those with a moderate amount of OVs [251]. Excessive OVs may introduce a new impurity band with unlocalized MO that can capture electrons excited from the VB and prevent them from arriving in the CB, thus decreasing the electronic conductivity [51,252]. Lately, researchers start to realize that OVs may differ in their locations (on the surface or in the bulk lattice). It is generally believed that the surface OVs contribute to catalytic activity whereas the bulk OVs act as a charge capture center to impede electron transfer [232]. Lv *et al.* [107] found that the surface OVs greatly improve the photocatalytic performance of $BiPO_{4-x}$ and enhance its response to visible light by broadening the VB and narrowing the band gap, whereas the bulk OVs act as the charge capture center and inhibit electron-hole separation. Nonetheless, the bulk OVs are also considered to play a positive role in boosting visible light harvesting, narrowing E_g, and slightly restraining the recombination

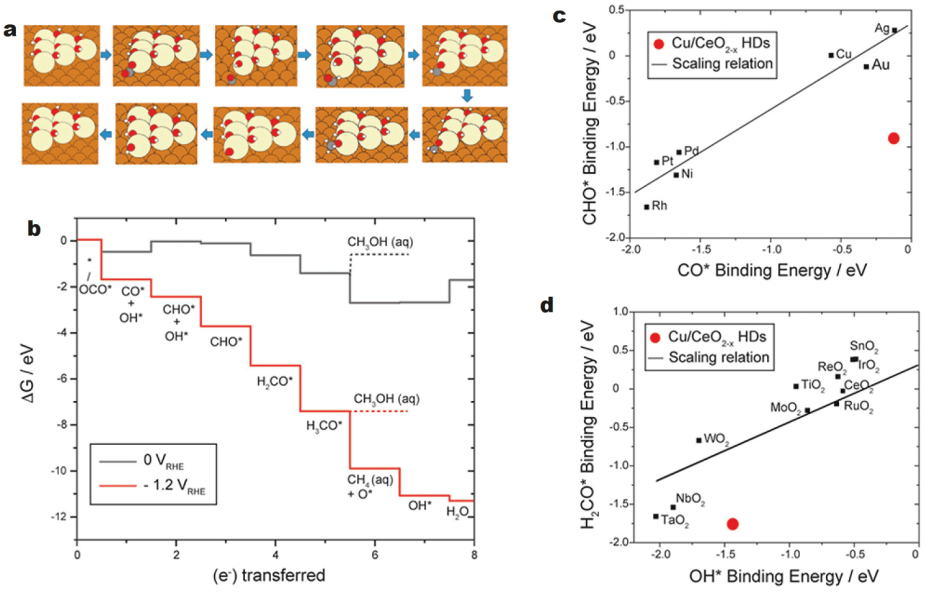

Figure 23 (a) CO_2 reduction on Cu/CeO_{2-x} heterodimers (HDs) for methane evolution at the active sites on the interface; (b) thermodynamics of methane and methanol evolution at 0 and $-1.2V_{RHE}$; (c, d) scaling relationship of CO*/CHO* and H_2CO*/OH* is broken due to a unique bidentate adsorption. Adapted with permission from Ref. [259], Copyright 2019, American Chemical Society.

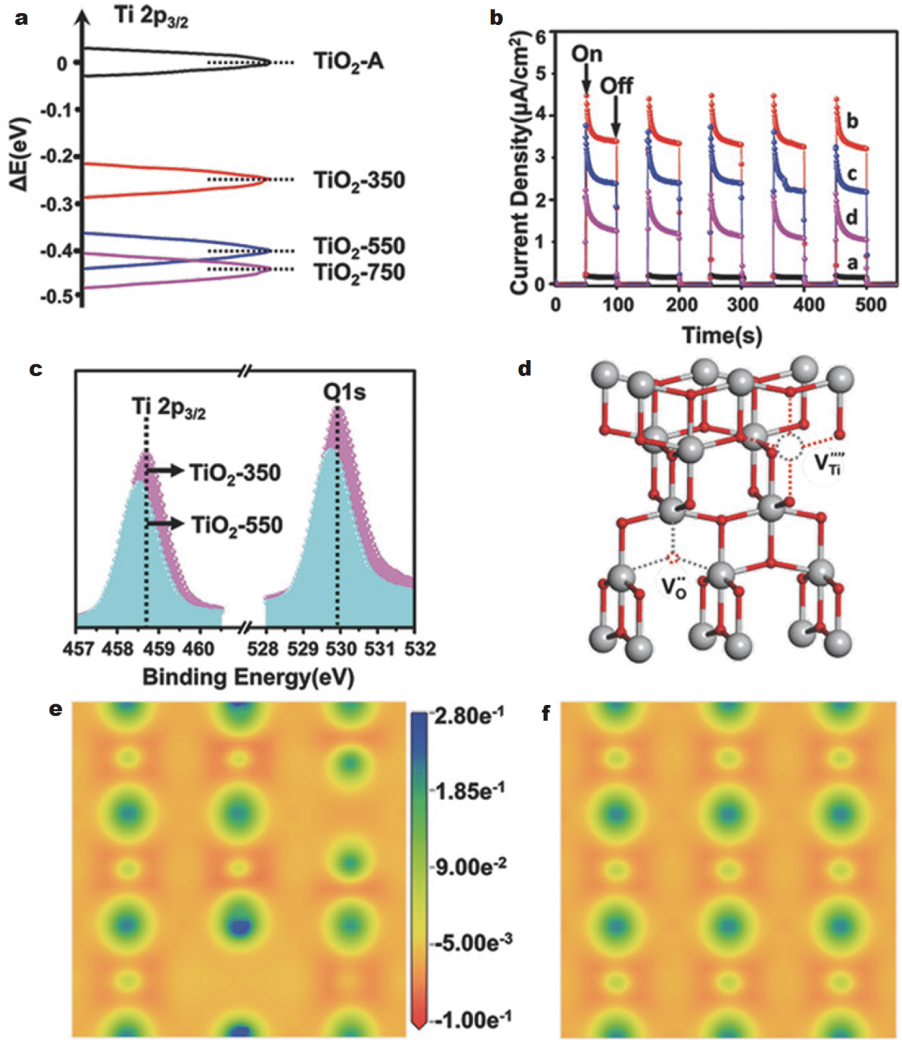

Figure 24 (a) The chemical shift of Ti $2p_{3/2}$ for TiO_2-A, TiO_2-350, TiO_2-550, and TiO_2-750; (b) the transient photocurrent responses of TiO_2-A, TiO_2-350, TiO_2-550, and TiO_2-750 *vs.* SCE under UV-vis irradiation; (c) Ti $2p_{3/2}$ and O 1s XPS spectra of TiO_2-350 and TiO_2-550; (d) simulated geometric structures of TiO_2 with junction of O vacancies and Ti vacancies; (e) charge density difference between normal TiO_2 and TiO_2 with junction of OVs and Ti vacancies. Adapted with permission from Ref. [297], Copyright 2018, WILEY-VCH Verlag GmbH & Co. KGaA, Weinheim.

of electrons and holes [298,299].

Because OVs in designed systems often exhibit multiple optical, electrical, and catalytic functions, the specific impact of OVs on catalysis is at times elusive and controversial. As such, conflicting findings are not uncommon regarding the connection between OVs and catalyst properties.

Identification of the real active sites of OVs-rich catalyst is also crucial for effective catalyst design. For instance, numerous studies suggested that OVs can be created by ion doping and the newly-formed OVs contributed to catalytic activity, but it remained controversial in some cases whether the OVs or the dopant ions were the active sites. More control experiments and systematic investigations are needed to identify the contribution of dopant to thus clearly establish the roles of OVs in the catalytic reaction. It is also worth mentioning that a synergy may exist between OVs and dopant ions to improve the catalytic activity [300,301].

Stability is a significant feature of advanced catalysts, but OVs are subject to oxidation during catalytic reactions, which can reduce catalytic activity. Surface OVs can be refilled when the oxides seize O atoms from water or molecular oxygen to render the original OV-free composition [302]. A number of strategies have been proposed to address the susceptibility of OVs to oxidation

[303,304]. For instance, Wang *et al.* [304] found that carbon coating can stabilize the surface OVs of TiO_2 nanorods [303]. Ion doping has also been adopted to stabilize OVs. However, a general approach to stabilize OVs in catalytic reactions is still lacking. A fundamental understanding of how the structural factors of the catalyst (e.g., size, lattice strain, dimension, surface structure, etc.) impact the stability of OVs is essential.

To summarize, challenges and opportunities abound in the exploration of advanced OVs-mediated photocatalysts. As the old saying goes, where there is a will, there is a way. Progress in this field can considerably improve the understanding of point defects and the design of related materials, and eventually help secure clean energy and lead to breakthroughs in environmental applications.

Received 20 January 2020; accepted 17 March 2020; published online 19 May 2020

1 Kong M, Li Y, Chen X, *et al.* Tuning the relative concentration ratio of bulk defects to surface defects in TiO_2 nanocrystals leads to high photocatalytic efficiency. J Am Chem Soc, 2011, 133: 16414–16417
2 Xu F, Zhu B, Cheng B, *et al.* 1D/2D TiO_2/MoS_2 hybrid nanostructures for enhanced photocatalytic CO_2 reduction. Adv Opt Mater, 2018, 6: 1800911
3 Xu Z, Yu J. Visible-light-induced photoelectrochemical behaviors of Fe-modified TiO_2 nanotube arrays. Nanoscale, 2011, 3: 3138–3144
4 Low J, Dai B, Tong T, *et al. In situ* irradiated X-ray photoelectron spectroscopy investigation on a direct Z-scheme TiO_2/CdS composite film photocatalyst. Adv Mater, 2019, 31: 1802981
5 Xu Z, Zheng R, Chen Y, *et al.* Ordered mesoporous Fe/TiO_2 with light enhanced photo-Fenton activity. Chin J Catal, 2019, 40: 631–637
6 Hüttenhofer L, Eckmann F, Lauri A, *et al.* Anapole excitations in oxygen-vacancy-rich TiO_{2-x} nanoresonators: tuning the absorption for photocatalysis in the visible spectrum. ACS Nano, 2020, 14: 2456–2464
7 Wan J, Chen W, Jia C, *et al.* Defect effects on TiO_2 nanosheets: stabilizing single atomic site Au and promoting catalytic properties. Adv Mater, 2018, 30: 1705369
8 Li X, Liu S, Fan K, *et al.* MOF-based transparent passivation layer modified ZnO nanorod arrays for enhanced photo-electrochemical water splitting. Adv Energy Mater, 2018, 8: 1800101
9 Yu W, Zhang J, Peng T. New insight into the enhanced photocatalytic activity of N-, C- and S-doped ZnO photocatalysts. Appl Catal B-Environ, 2016, 181: 220–227
10 Kim HS, Cook JB, Lin H, *et al.* Oxygen vacancies enhance pseudocapacitive charge storage properties of MoO_{3-x}. Nat Mater, 2017, 16: 454–460
11 Xu Q, Zhu B, Jiang C, *et al.* Constructing 2D/2D Fe_2O_3/g-C_3N_4 direct Z-scheme photocatalysts with enhanced H_2 generation performance. Sol RRL, 2018, 2: 1800006
12 Auxilia FM, Ishihara S, Mandal S, *et al.* Low-temperature remediation of NO catalyzed by interleaved CuO nanoplates. Adv Mater, 2014, 26: 4481–4485
13 Gu Z, Yang N, Han P, *et al.* Oxygen vacancy tuning toward efficient electrocatalytic CO_2 reduction to C_2H_4. Small Methods, 2018, 3: 1800449
14 Guo S, Jiang Y, Li L, *et al.* Thin CuO_x-based nanosheets for efficient phenol removal benefitting from structural memory and ion exchange of layered double oxides. J Mater Chem A, 2018, 6: 4167–4178
15 Pastrián FAC, da Silva AGM, Dourado AHB, *et al.* Why could the nature of surface facets lead to differences in the activity and stability of Cu_2O-based electrocatalytic sensors? ACS Catal, 2018, 8: 6265–6272
16 Lee S, Nam G, Sun J, *et al.* Enhanced intrinsic catalytic activity of λ-MnO_2 by electrochemical tuning and oxygen vacancy generation. Angew Chem Int Ed, 2016, 55: 8599–8604
17 Wang X, Zhou Z, Liang Z, *et al.* Photochemical synthesis of the $Fe^0/C_3N_4/MoS_2$ heterostructure as a highly active and reusable photocatalyst. Appl Surf Sci, 2017, 423: 225–235
18 Chen S, Wang X, Fan L, *et al.* The dynamic phase transition modulation of ion-liquid gating VO_2 thin film: formation, diffusion, and recovery of oxygen vacancies. Adv Funct Mater, 2016, 26: 3532–3541
19 Hou T, Xiao Y, Cui P, *et al. Operando* oxygen vacancies for enhanced activity and stability toward nitrogen photofixation. Adv Energy Mater, 2019, 9: 1902319
20 Jia K, Ye J, Zhuang G, *et al.* Well-defined $Cu_2O/Cu_3(BTC)_2$ sponge architecture as efficient phenolics scavenger: synchronous etching and reduction of MOFs in confined-pH $NH_3{\cdot}H_2O$. Small, 2019, 15: 1805478
21 Ma L, Chen S, Pei Z, *et al.* Flexible waterproof rechargeable hybrid zinc batteries initiated by multifunctional oxygen vacancies-rich cobalt oxide. ACS Nano, 2018, 12: 8597–8605
22 Sun Y, Wang H, Xing Q, *et al.* The pivotal effects of oxygen vacancy on Bi_2MoO_6: Promoted visible light photocatalytic activity and reaction mechanism. Chin J Catal, 2019, 40: 647–655
23 Ortiz-Medina J, Wang Z, Cruz-Silva R, *et al.* Defect engineering and surface functionalization of nanocarbons for metal-free catalysis. Adv Mater, 2019, 31: 1805717
24 Tompkins FC. Superficial chemistry and solid imperfections. Nature, 1960, 186: 3–6
25 Deb SK, Chopoorian JA. Optical properties and color-center formation in thin films of molybdenum trioxide. J Appl Phys, 1966, 37: 4818–4825
26 Tohmon R, Mizuno H, Ohki Y, *et al.* Correlation of the 5.0- and 7.6-eV absorption bands in SiO_2 with oxygen vacancy. Phys Rev B, 1989, 39: 1337–1345
27 Kevane CJ. Oxygen vacancies and electrical conduction in metal oxides. Phys Rev, 1964, 133: A1431–A1436
28 Sawada H, Kawakami K. Electronic structure of oxygen vacancy in Ta_2O_5. J Appl Phys, 1999, 86: 956–959
29 Hughes AE. Production of oxygen vacancies by elastic collisions in alkaline earth oxides. J Phys Colloques, 1973, 34: C9-515–C9-518
30 Iguchi E, Yajima K. Diffusion of oxygen vacancies in reduced rutile (TiO_2). J Phys Soc Jpn, 1972, 32: 1415–1421
31 Metselaar R, Larsen PK. Diffusion of oxygen vacancies in yttrium iron garnet investigated by dynamic conductivity measurements. J Phys Chem Solids, 1976, 37: 599–605
32 Over H, Kim YD, Seitsonen AP, *et al.* Atomic-scale structure and catalytic reactivity of the RuO_2(110) surface. Science, 2000, 287:

1474–1476
33 Jiang Y. Kinetic study of the formation of oxygen vacancy on lanthanum manganite electrodes. J Electrochem Soc, 1998, 145: 373
34 Chen X, Liu L, Yu PY, *et al.* Increasing solar absorption for photocatalysis with black hydrogenated titanium dioxide nanocrystals. Science, 2011, 331: 746–750
35 Ou G, Xu Y, Wen B, *et al.* Tuning defects in oxides at room temperature by lithium reduction. Nat Commun, 2018, 9: 1302
36 Wang G, Ling Y, Wang H, *et al.* Hydrogen-treated WO_3 nanoflakes show enhanced photostability. Energy Environ Sci, 2012, 5: 6180–6187
37 Kropp T, Lu Z, Li Z, *et al.* Anionic single-atom catalysts for CO oxidation: support-independent activity at low temperatures. ACS Catal, 2019, 9: 1595–1604
38 Liu Y, Cheng H, Lyu M, *et al.* Low overpotential in vacancy-rich ultrathin $CoSe_2$ nanosheets for water oxidation. J Am Chem Soc, 2014, 136: 15670–15675
39 Bao J, Zhang X, Fan B, *et al.* Ultrathin spinel-structured nanosheets rich in oxygen deficiencies for enhanced electrocatalytic water oxidation. Angew Chem Int Ed, 2015, 54: 7399–7404
40 Rodriguez JA, Ma S, Liu P, *et al.* Activity of CeO_x and TiO_x nanoparticles grown on Au(111) in the water-gas shift reaction. Science, 2007, 318: 1757–1760
41 Liu X, Zhou K, Wang L, *et al.* Oxygen vacancy clusters promoting reducibility and activity of ceria nanorods. J Am Chem Soc, 2009, 131: 3140–3141
42 Maimaiti Y, Nolan M, Elliott SD. Reduction mechanisms of the CuO(111) surface through surface oxygen vacancy formation and hydrogen adsorption. Phys Chem Chem Phys, 2014, 16: 3036–3046
43 Dvořák F, Szabová L, Johánek V, *et al.* Bulk hydroxylation and effective water splitting by highly reduced cerium oxide: the role of O vacancy coordination. ACS Catal, 2018, 8: 4354–4363
44 Corby S, Francàs L, Selim S, *et al.* Water oxidation and electron extraction kinetics in nanostructured tungsten trioxide photoanodes. J Am Chem Soc, 2018, 140: 16168–16177
45 Qi L, Yu Q, Dai Y, *et al.* Influence of cerium precursors on the structure and reducibility of mesoporous CuO-CeO_2 catalysts for CO oxidation. Appl Catal B-Environ, 2012, 119-120: 308–320
46 Saavedra J, Pursell CJ, Chandler BD. CO oxidation kinetics over Au/TiO_2 and Au/Al_2O_3 catalysts: evidence for a common water-assisted mechanism. J Am Chem Soc, 2018, 140: 3712–3723
47 He C, Yu Y, Shen Q, *et al.* Catalytic behavior and synergistic effect of nanostructured mesoporous CuO-MnO_x-CeO_2 catalysts for chlorobenzene destruction. Appl Surf Sci, 2014, 297: 59–69
48 Wang Z, Wen B, Hao Q, *et al.* Localized excitation of Ti^{3+} ions in the photoabsorption and photocatalytic activity of reduced rutile TiO_2. J Am Chem Soc, 2015, 137: 9146–9152
49 Wang H, Yong D, Chen S, *et al.* Oxygen-vacancy-mediated exciton dissociation in BiOBr for boosting charge-carrier-involved molecular oxygen activation. J Am Chem Soc, 2018, 140: 1760–1766
50 Tong H, Ouyang S, Bi Y, *et al.* Nano-photocatalytic materials: possibilities and challenges. Adv Mater, 2012, 24: 229–251
51 Kotiuga M, Zhang Z, Li J, *et al.* Carrier localization in perovskite nickelates from oxygen vacancies. Proc Natl Acad Sci USA, 2019, 116: 21992–21997
52 Vikrant KSN, Chueh WC, García RE. Charged interfaces: electrochemical and mechanical effects. Energy Environ Sci, 2018, 11: 1993–2000
53 Liu L, Mei Z, Tang A, *et al.* Oxygen vacancies: The origin of n-type conductivity in ZnO. Phys Rev B, 2016, 93: 235305
54 Develos-Bagarinao K, De Vero J, Kishimoto H, *et al.* Multilayered LSC and GDC: an approach for designing cathode materials with superior oxygen exchange properties for solid oxide fuel cells. Nano Energy, 2018, 52: 369–380
55 Huo WC, Dong X, Li JY, *et al.* Synthesis of Bi_2WO_6 with gradient oxygen vacancies for highly photocatalytic NO oxidation and mechanism study. Chem Eng J, 2019, 361: 129–138
56 Chen CF, King G, Dickerson RM, *et al.* Oxygen-deficient $BaTiO_{3-x}$ perovskite as an efficient bifunctional oxygen electrocatalyst. Nano Energy, 2015, 13: 423–432
57 Campbell CT. Waltzing with O_2. Science, 2003, 299: 357
58 Rasmussen MD, Molina LM, Hammer B. Adsorption, diffusion, and dissociation of molecular oxygen at defected TiO_2(110): a density functional theory study. J Chem Phys, 2004, 120: 988–997
59 Ye J, Liu C, Mei D, *et al.* Active oxygen vacancy site for methanol synthesis from CO_2 hydrogenation on In_2O_3 (110): A DFT study. ACS Catal, 2013, 3: 1296–1306
60 Zhao Y, Zhao Y, Shi R, *et al.* Tuning oxygen vacancies in ultrathin TiO_2 nanosheets to boost photocatalytic nitrogen fixation up to 700 nm. Adv Mater, 2019, 31: 1806482
61 Deml AM, Stevanović V, Muhich CL, *et al.* Oxide enthalpy of formation and band gap energy as accurate descriptors of oxygen vacancy formation energetics. Energy Environ Sci, 2014, 7: 1996–2004
62 Xu L, Jiang Q, Xiao Z, *et al.* Plasma-engraved Co_3O_4 nanosheets with oxygen vacancies and high surface area for the oxygen evolution reaction. Angew Chem Int Ed, 2016, 55: 5277–5281
63 Park B, Ho D, Kwon G, *et al.* Solution-processed rad-hard amorphous metal-oxide thin-film transistors. Adv Funct Mater, 2018, 28: 1802717
64 Wu J, Li X, Shi W, *et al.* Efficient visible-light-driven CO_2 reduction mediated by defect-engineered BiOBr atomic layers. Angew Chem, 2018, 130: 8855–8859
65 Tao L, Shi Y, Huang YC, *et al.* Interface engineering of Pt and CeO_2 nanorods with unique interaction for methanol oxidation. Nano Energy, 2018, 53: 604–612
66 Chen G, Georgieva V, Godfroid T, *et al.* Plasma assisted catalytic decomposition of CO_2. Appl Catal B-Environ, 2016, 190: 115–124
67 Pan J, Ganesan R, Shen H, *et al.* Plasma-modified SnO_2 nanowires for enhanced gas sensing. J Phys Chem C, 2010, 114: 8245–8250
68 Bruno FY, Tornos J, Gutierrez del Olmo M, *et al.* Anisotropic magnetotransport in $SrTiO_3$ surface electron gases generated by Ar^+ irradiation. Phys Rev B, 2011, 83: 245120
69 Brusa RS, Karwasz GP, Mariotto G, *et al.* Structural evolution in Ar^+ implanted Si-rich silicon oxide. J Appl Phys, 2003, 94: 7483–7492
70 Zhu C, Li C, Zheng M, *et al.* Plasma-induced oxygen vacancies in ultrathin hematite nanoflakes promoting photoelectrochemical water oxidation. ACS Appl Mater Interfaces, 2015, 7: 22355–22363
71 Bose S, Mandal S, Barua AK, *et al.* Properties of boron doped ZnO films prepared by reactive sputtering method: application to amorphous silicon thin film solar cells. J Mater Sci Tech, 2019
72 Kuwahara Y, Yoshimura Y, Haematsu K, *et al.* Mild deoxygenation of sulfoxides over plasmonic molybdenum oxide hybrid with dramatic activity enhancement under visible light. J Am Chem Soc, 2018, 140: 9203–9210

73 Qi K, Cheng B, Yu J, *et al.* Review on the improvement of the photocatalytic and antibacterial activities of ZnO. J Alloys Compd, 2017, 727: 792–820
74 Fujita T, Ishida T, Shibamoto K, *et al.* CO oxidation over Au/ZnO: Unprecedented change of the reaction mechanism at low temperature caused by a different O_2 activation process. ACS Catal, 2019, 9: 8364–8372
75 Faisal M, Khan SB, Rahman MM, *et al.* Role of ZnO-CeO_2 nanostructures as a photo-catalyst and chemi-sensor. J Mater Sci Tech, 2011, 27: 594–600
76 Meng L, Tian W, Wu F, *et al.* TiO_2 ALD decorated CuO/$BiVO_4$ p-n heterojunction for improved photoelectrochemical water splitting. J Mater Sci Tech, 2019, 35: 1740–1746
77 Liu C, Zhu X, Wang P, *et al.* Defects and interface states related photocatalytic properties in reduced and subsequently nitridized Fe_3O_4/TiO_2. J Mater Sci Tech, 2018, 34: 931–941
78 Zhou P, Wu J, Yu W, *et al.* Vectorial doping-promoting charge transfer in anatase TiO_2 {001} surface. Appl Surf Sci, 2014, 319: 167–172
79 Liu J, Li N, Dong Q, *et al.* Tailoring electrical property of the low-temperature processed SnO_2 for high-performance perovskite solar cells. Sci China Mater, 2019, 62: 173–180
80 Ye KH, Wang Z, Li H, *et al.* A novel CoOOH/(Ti,C)-Fe_2O_3 nanorod photoanode for photoelectrochemical water splitting. Sci China Mater, 2018, 61: 887–894
81 Feibelman PJ, Knotek ML. Reinterpretation of electron-stimulated desorption data from chemisorption systems. Phys Rev B, 1978, 18: 6531–6539
82 von Soosten M, Christensen DV, Eom CB, *et al.* On the emergence of conductivity at $SrTiO_3$-based oxide interfaces—an *in-situ* study. Sci Rep, 2019, 9: 1–7
83 Hou J, Cao S, Wu Y, *et al.* Perovskite-based nanocubes with simultaneously improved visible-light absorption and charge separation enabling efficient photocatalytic CO_2 reduction. Nano Energy, 2016, 30: 59–68
84 Lv K, Xiang Q, Yu J. Effect of calcination temperature on morphology and photocatalytic activity of anatase TiO_2 nanosheets with exposed {001} facets. Appl Catal B-Environ, 2011, 104: 275–281
85 Xu HY, Huang YH, Liu S, *et al.* Effects of annealing ambient on oxygen vacancies and phase transition temperature of VO_2 thin films. RSC Adv, 2016, 6: 79383–79388
86 Hou L, Zhang M, Guan Z, *et al.* Effect of annealing ambience on the formation of surface/bulk oxygen vacancies in TiO_2 for photocatalytic hydrogen evolution. Appl Surf Sci, 2018, 428: 640–647
87 Liang Q, Guo Y, Zhang N, *et al.* Improved water-splitting performances of $CuW_{1-x}Mo_xO_4$ photoanodes synthesized by spray pyrolysis. Sci China Mater, 2018, 61: 1297–1304
88 Schlexer P, Widmann D, Behm RJ, *et al.* CO oxidation on a Au/TiO_2 nanoparticle catalyst *via* the Au-assisted Mars–van Krevelen mechanism. ACS Catal, 2018, 8: 6513–6525
89 Tong Y, Chen P, Zhang M, *et al.* Oxygen vacancies confined in nickel molybdenum oxide porous nanosheets for promoted electrocatalytic urea oxidation. ACS Catal, 2018, 8: 1–7
90 Dawson JA, Chen H, Tanaka I. First-principles calculations of oxygen vacancy formation and metallic behavior at a β-MnO_2 grain boundary. ACS Appl Mater Interfaces, 2015, 7: 1726–1734
91 Tan H, Zhao Z, Zhu WB, *et al.* Oxygen vacancy enhanced photocatalytic activity of pervoskite $SrTiO_3$. ACS Appl Mater Interfaces, 2014, 6: 19184–19190
92 Jaiswar S, Mandal KD. Evidence of enhanced oxygen vacancy defects inducing ferromagnetism in multiferroic $CaMn_7O_{12}$ manganite with sintering time. J Phys Chem C, 2017, 121: 19586–19601
93 Jiang ZL, Xu GL, Yu Z, *et al.* High rate and long cycle life in Li-O_2 batteries with highly efficient catalytic cathode configured with Co_3O_4 nanoflower. Nano Energy, 2019, 64: 103896
94 Santara B, Giri PK, Imakita K, *et al.* Evidence of oxygen vacancy induced room temperature ferromagnetism in solvothermally synthesized undoped TiO_2 nanoribbons. Nanoscale, 2013, 5: 5476–5488
95 Zhang W, Cai L, Cao S, *et al.* Interfacial lattice-strain-driven generation of oxygen vacancies in an aerobic-annealed TiO_2(B) electrode. Adv Mater, 2019, 31: 1906156
96 Liu WT, Wu BH, Lai YT, *et al.* Enhancement of water splitting by controlling the amount of vacancies with varying vacuum level in the synthesis system of SnO_{2-x}/In_2O_{3-y} heterostructure as photocatalyst. Nano Energy, 2018, 47: 18–25
97 Lv Y, Pan C, Ma X, *et al.* Production of visible activity and UV performance enhancement of ZnO photocatalyst *via* vacuum deoxidation. Appl Catal B-Environ, 2013, 138-139: 26–32
98 Yang J, Lee J, Lee J, *et al.* Oxygen annealing of the ZnO nanoparticle layer for the high-performance PbS colloidal quantum-dot photovoltaics. J Power Sources, 2019, 421: 124–131
99 Zhu G, Zhu J, Jiang W, *et al.* Surface oxygen vacancy induced α-MnO_2 nanofiber for highly efficient ozone elimination. Appl Catal B-Environ, 2017, 209: 729–737
100 Xing M, Zhang J, Chen F, *et al.* An economic method to prepare vacuum activated photocatalysts with high photo-activities and photosensitivities. Chem Commun, 2011, 47: 4947–4949
101 Liu D, Wang C, Yu Y, *et al.* Understanding the nature of ammonia treatment to synthesize oxygen vacancy-enriched transition metal oxides. Chem, 2019, 5: 376–389
102 He W, Sun Y, Jiang G, *et al.* Defective Bi_4MoO_9/Bi metal core/shell heterostructure: enhanced visible light photocatalysis and reaction mechanism. Appl Catal B-Environ, 2018, 239: 619–627
103 Lee L, Kang B, Han S, *et al.* A generalizable top-down nanostructuring method of bulk oxides: sequential oxygen-nitrogen exchange reaction. Small, 2018, 14: 1801124
104 Zhou X, Shen Q, Yuan K, *et al.* Unraveling charge state of supported Au single-atoms during CO oxidation. J Am Chem Soc, 2018, 140: 554–557
105 Selcuk S, Zhao X, Selloni A. Structural evolution of titanium dioxide during reduction in high-pressure hydrogen. Nat Mater, 2018, 17: 923–928
106 Bielz T, Lorenz H, Jochum W, *et al.* Hydrogen on In_2O_3: Reducibility, bonding, defect formation, and reactivity. J Phys Chem C, 2010, 114: 9022–9029
107 Lv Y, Liu Y, Zhu Y, *et al.* Surface oxygen vacancy induced photocatalytic performance enhancement of a $BiPO_4$ nanorod. J Mater Chem A, 2014, 2: 1174–1182
108 Zhu G, Lin T, Lü X, *et al.* Black brookite titania with high solar absorption and excellent photocatalytic performance. J Mater Chem A, 2013, 1: 9650–9653
109 Amano F, Nakata M. High-temperature calcination and hydrogen reduction of rutile TiO_2: a method to improve the photocatalytic activity for water oxidation. Appl Catal B-Environ, 2014, 158-159: 202–208
110 Wang Y, Feng C, Zhang M, *et al.* Enhanced visible light photo-

catalytic activity of N-doped TiO_2 in relation to single-electron-trapped oxygen vacancy and doped-nitrogen. Appl Catal B-Environ, 2010, 100: 84–90
111 Liu K, Zhang W, Lei F, *et al.* Nitrogen-doping induced oxygen divacancies in freestanding molybdenum trioxide single-layers boosting electrocatalytic hydrogen evolution. Nano Energy, 2016, 30: 810–817
112 Maqbool Q, Srivastava A. Benign synthesis of black microspheres of anatase TiO_2 with paramagnetic oxygen vacancies through NH_3 treatment. Chem Eur J, 2017, 23: 13864–13868
113 Chen H, Yang M, Tao S, *et al.* Oxygen vacancy enhanced catalytic activity of reduced Co_3O_4 towards *p*-nitrophenol reduction. Appl Catal B-Environ, 2017, 209: 648–656
114 Zhuang L, Ge L, Yang Y, *et al.* Ultrathin iron-cobalt oxide nanosheets with abundant oxygen vacancies for the oxygen evolution reaction. Adv Mater, 2017, 29: 1606793
115 Li J, Liang Z, Guo L, *et al.* Flower-like Bi_2WO_6 with oxygen vacancies achieving enhanced photoelectrocatalytic performance. Mater Lett, 2018, 223: 93–96
116 Yang J, Hu S, Fang Y, *et al.* Oxygen vacancy promoted O_2 activation over perovskite oxide for low-temperature CO oxidation. ACS Catal, 2019, 9: 9751–9763
117 Werner K, Weng X, Calaza F, *et al.* Toward an understanding of selective alkyne hydrogenation on ceria: on the impact of O vacancies on H_2 interaction with CeO_2 (111). J Am Chem Soc, 2017, 139: 17608–17616
118 Xu W, Lyu F, Bai Y, *et al.* Porous cobalt oxide nanoplates enriched with oxygen vacancies for oxygen evolution reaction. Nano Energy, 2018, 43: 110–116
119 Bai Y, Ye L, Chen T, *et al.* Facet-dependent photocatalytic N_2 fixation of bismuth-rich Bi_5O_7I nanosheets. ACS Appl Mater Interfaces, 2016, 8: 27661–27668
120 Cai Z, Bi Y, Hu E, *et al.* Single-crystalline ultrathin Co_3O_4 nanosheets with massive vacancy defects for enhanced electrocatalysis. Adv Energy Mater, 2018, 8: 1701694
121 Li X, Ma J, Yang L, *et al.* Oxygen vacancies induced by transition metal doping in γ-MnO_2 for highly efficient ozone decomposition. Environ Sci Technol, 2018, 52: 12685–12696
122 Jia J, Zhang P, Chen L. Catalytic decomposition of gaseous ozone over manganese dioxides with different crystal structures. Appl Catal B-Environ, 2016, 189: 210–218
123 Baeumer C, Funck C, Locatelli A, *et al.* In-gap states and band-like transport in memristive devices. Nano Lett, 2018, 19: 54–60
124 Setvín M, Aschauer U, Scheiber P, *et al.* Reaction of O_2 with subsurface oxygen vacancies on TiO_2 anatase (101). Science, 2013, 341: 988–991
125 Tsai MC, Nguyen TT, Akalework NG, *et al.* Interplay between molybdenum dopant and oxygen vacancies in a TiO_2 support enhances the oxygen reduction reaction. ACS Catal, 2016, 6: 6551–6559
126 Wei J, Cheng N, Liang Z, *et al.* Heterometallic metal–organic framework nanocages of high crystallinity: an elongated channel structure formed *in situ* through metal-ion (M = W or Mo) doping. J Mater Chem A, 2018, 6: 23336–23344
127 Jiang H, Liu J, Li M, *et al.* Facile synthesis of C-decorated Fe, N co-doped TiO_2 with enhanced visible-light photocatalytic activity by a novel co-precursor method. Chin J Catal, 2018, 39: 747–759
128 Kim JK, Chai SU, Ji Y, *et al.* Resolving hysteresis in perovskite solar cells with rapid flame-processed cobalt-doped TiO_2. Adv Energy Mater, 2018, 8: 1801717
129 Nolan M. Enhanced oxygen vacancy formation in ceria (111) and (110) surfaces doped with divalent cations. J Mater Chem, 2011, 21: 9160–9168
130 Wang Z, You Y, Yuan J, *et al.* Nickel-doped $La_{0.8}Sr_{0.2}Mn_{1-x}Ni_xO_3$ nanoparticles containing abundant oxygen vacancies as an optimized bifunctional catalyst for oxygen cathode in rechargeable lithium–air batteries. ACS Appl Mater Interfaces, 2016, 8: 6520–6528
131 Zhang T, Wu MY, Yan DY, *et al.* Engineering oxygen vacancy on NiO nanorod arrays for alkaline hydrogen evolution. Nano Energy, 2018, 43: 103–109
132 Ling T, Yan DY, Jiao Y, *et al.* Engineering surface atomic structure of single-crystal cobalt (II) oxide nanorods for superior electrocatalysis. Nat Commun, 2016, 7: 12876
133 Wang Y, Chen Z, Han P, *et al.* Single-atomic Cu with multiple oxygen vacancies on ceria for electrocatalytic CO_2 reduction to CH_4. ACS Catal, 2018, 8: 7113–7119
134 Chen C, Xu K, Ji X, *et al.* Enhanced electrochemical performance by facile oxygen vacancies from lower valence-state doping for ramsdellite-MnO_2. J Mater Chem A, 2015, 3: 12461–12467
135 McFarland EW, Metiu H. Catalysis by doped oxides. Chem Rev, 2013, 113: 4391–4427
136 Wang J, Tafen DN, Lewis JP, *et al.* Origin of photocatalytic activity of nitrogen-doped TiO_2 nanobelts. J Am Chem Soc, 2009, 131: 12290–12297
137 Hensel J, Wang G, Li Y, *et al.* Synergistic effect of CdSe quantum dot sensitization and nitrogen doping of TiO_2 nanostructures for photoelectrochemical solar hydrogen generation. Nano Lett, 2010, 10: 478–483
138 Tang K, Mu X, van Aken PA, *et al.* "Nano-pearl-string" $TiNb_2O_7$ as anodes for rechargeable lithium batteries. Adv Energy Mater, 2013, 3: 49–53
139 Meng Y, Chen J, Wang Y, *et al.* (N, F)-codoped TiO_2 nanocrystals as visible light-activated photocatalyst. J Mater Sci Technol, 2009, 25: 73–76
140 Li X, Wei J, Li Q, *et al.* Nitrogen-doped cobalt oxide nanostructures derived from cobalt-alanine complexes for high-performance oxygen evolution reactions. Adv Funct Mater, 2018, 28: 1800886
141 Sun Z, Xu L, Dong C, *et al.* A facile gaseous sulfur treatment strategy for Li-rich and Ni-rich cathode materials with high cycling and rate performance. Nano Energy, 2019, 63: 103887
142 Sun J, Guo N, Shao Z, *et al.* A Facile strategy to construct amorphous spinel-based electrocatalysts with massive oxygen vacancies using ionic liquid dopant. Adv Energy Mater, 2018, 8: 1800980
143 Qu Z, Bu Y, Qin Y, *et al.* The improved reactivity of manganese catalysts by Ag in catalytic oxidation of toluene. Appl Catal B-Environ, 2013, 132-133: 353–362
144 Schilling C, Hess C. Elucidating the role of support oxygen in the water–gas shift reaction over ceria-supported gold catalysts using *operando* spectroscopy. ACS Catal, 2018, 9: 1159–1171
145 Hare BJ, Maiti D, Daza YA, *et al.* Enhanced CO_2 conversion to CO by silica-supported perovskite oxides at low temperatures. ACS Catal, 2018, 8: 3021–3029
146 Nolan M, Deskins NA, Schwartzenberg KC, *et al.* Local interfacial structure influences charge localization in titania composites: beyond the band alignment paradigm. J Phys Chem C, 2016, 120: 1808–1815
147 Seok TJ, Liu Y, Jung HJ, *et al.* Field-effect device using quasi-two-

dimensional electron gas in mass-producible atomic-layer-deposited Al_2O_3/TiO_2 ultrathin (<10 nm) film heterostructures. ACS Nano, 2018, 12: 10403–10409
148 Zhong Z, Xu PX, Kelly PJ. Polarity-induced oxygen vacancies at $LaAlO_3/SrTiO_3$ interfaces. Phys Rev B, 2010, 82: 165127
149 Qiu B, Wang C, Zhang N, *et al.* CeO_2-induced interfacial Co^{2+} octahedral sites and oxygen vacancies for water oxidation. ACS Catal, 2019, 9: 6484–6490
150 Veal BW, Kim SK, Zapol P, *et al.* Interfacial control of oxygen vacancy doping and electrical conduction in thin film oxide heterostructures. Nat Commun, 2016, 7: 11892
151 Zhou Y, Zhang Z, Fang Z, *et al.* Defect engineering of metal–oxide interface for proximity of photooxidation and photoreduction. Proc Natl Acad Sci USA, 2019, 116: 10232–10237
152 Yang Z, Lu Z, Luo G, *et al.* Oxygen vacancy formation energy at the $Pd/CeO_2(111)$ interface. Phys Lett A, 2007, 369: 132–139
153 Chen S, Li L, Hu W, *et al.* Anchoring high-concentration oxygen vacancies at interfaces of CeO_{2-x}/Cu toward enhanced activity for preferential CO oxidation. ACS Appl Mater Interfaces, 2015, 7: 22999–23007
154 Gac W, Giecko G, Pasieczna-Patkowska S, *et al.* The influence of silver on the properties of cryptomelane type manganese oxides in N_2O decomposition reaction. Catal Today, 2008, 137: 397–402
155 Ishida T, Murayama T, Taketoshi A, *et al.* Importance of size and contact structure of gold nanoparticles for the genesis of unique catalytic processes. Chem Rev, 2019, 120: 464–525
156 Riva M, Kubicek M, Hao X, *et al.* Influence of surface atomic structure demonstrated on oxygen incorporation mechanism at a model perovskite oxide. Nat Commun, 2018, 9: 3710
157 Michalsky R, Botu V, Hargus CM, *et al.* Design principles for metal oxide redox materials for solar-driven isothermal fuel production. Adv Energy Mater, 2015, 5: 1401082
158 Hayashi E, Yamaguchi Y, Kamata K, *et al.* Effect of MnO_2 crystal structure on aerobic oxidation of 5-hydroxymethylfurfural to 2,5-furandicarboxylic acid. J Am Chem Soc, 2019, 141: 890–900
159 Gorlin Y, Lassalle-Kaiser B, Benck JD, *et al. In situ* X-ray absorption spectroscopy investigation of a bifunctional manganese oxide catalyst with high activity for electrochemical water oxidation and oxygen reduction. J Am Chem Soc, 2013, 135: 8525–8534
160 Yu H, So YG, Ren Y, *et al.* Temperature-sensitive structure evolution of lithium–manganese-rich layered oxides for lithium-ion batteries. J Am Chem Soc, 2018, 140: 15279–15289
161 Weng Z, Li J, Weng Y, *et al.* Surfactant-free porous nano-Mn_3O_4 as a recyclable Fenton-like reagent that can rapidly scavenge phenolics without H_2O_2. J Mater Chem A, 2017, 5: 15650–15660
162 Li H, Shang H, Li Y, *et al.* Interfacial charging–decharging strategy for efficient and selective aerobic NO oxidation on oxygen vacancy. Environ Sci Technol, 2019, 53: 6964–6971
163 Hu L, Peng Q, Li Y. Selective synthesis of Co_3O_4 nanocrystal with different shape and crystal plane effect on catalytic property for methane combustion. J Am Chem Soc, 2008, 130: 16136–16137
164 Zhang KHL, Sushko PV, Colby R, *et al.* Reversible nano-structuring of $SrCrO_{3-\delta}$ through oxidation and reduction at low temperature. Nat Commun, 2014, 5: 4669
165 Xie Y, Wu J, Jing G, *et al.* Structural origin of high catalytic activity for preferential CO oxidation over CuO/CeO_2 nanocatalysts with different shapes. Appl Catal B-Environ, 2018, 239: 665–676
166 Tompsett DA, Parker SC, Islam MS. Rutile (β-)MnO_2 surfaces and vacancy formation for high electrochemical and catalytic performance. J Am Chem Soc, 2014, 136: 1418–1426
167 Huang W. Oxide nanocrystal model catalysts. Acc Chem Res, 2016, 49: 520–527
168 Wang B, Wang X, Lu L, *et al.* Oxygen-vacancy-activated CO_2 splitting over amorphous oxide semiconductor photocatalyst. ACS Catal, 2017, 8: 516–525
169 Xu Y, Zhou M, Zhang C, *et al.* Oxygen vacancies: effective strategy to boost sodium storage of amorphous electrode materials. Nano Energy, 2017, 38: 304–312
170 Gong L, Chng XYE, Du Y, *et al.* Enhanced catalysis of the electrochemical oxygen evolution reaction by iron(III) ions adsorbed on amorphous cobalt oxide. ACS Catal, 2017, 8: 807–814
171 Duan Y, Yu ZY, Hu SJ, *et al.* Scaled-up synthesis of amorphous NiFeMo oxides and their rapid surface reconstruction for superior oxygen evolution catalysis. Angew Chem Int Ed, 2019, 58: 15772–15777
172 Lim J, Kim SH, Aymerich Armengol R, *et al.* Atomic-scale mapping of impurities in partially reduced hollow TiO_2 nanowires. Angew Chem Int Ed, 2020, 59: 5651–5655
173 Cox JW, Foster GM, Jarjour A, *et al.* Defect manipulation to control ZnO micro-/nanowire-metal contacts. Nano Lett, 2018, 18: 6974–6980
174 Huang Y, Li K, Li S, *et al.* Ultrathin Bi_2MoO_6 nanosheets for photocatalysis: performance enhancement by atomic interfacial engineering. ChemistrySelect, 2018, 3: 7423–7428
175 Ding L, Wei R, Chen H, *et al.* Controllable synthesis of highly active BiOCl hierarchical microsphere self-assembled by nanosheets with tunable thickness. Appl Catal B-Environ, 2015, 172-173: 91–99
176 Liao L, Lu HB, Li JC, *et al.* Size dependence of gas sensitivity of ZnO nanorods. J Phys Chem C, 2007, 111: 1900–1903
177 Zhou XD, Huebner W. Size-induced lattice relaxation in CeO_2 nanoparticles. Appl Phys Lett, 2001, 79: 3512–3514
178 Petrie JR, Mitra C, Jeen H, *et al.* Strain control of oxygen vacancies in epitaxial strontium cobaltite films. Adv Funct Mater, 2016, 26: 1564–1570
179 Iglesias L, Sarantopoulos A, Magén C, *et al.* Oxygen vacancies in strained $SrTiO_3$ thin films: Formation enthalpy and manipulation. Phys Rev B, 2017, 95: 165138
180 Rahman MA, Thomas JP, Leung KT. A delaminated defect-rich ZrO_2 hierarchical nanowire photocathode for efficient photoelectrochemical hydrogen evolution. Adv Energy Mater, 2018, 8: 1701234
181 Riley C, Zhou S, Kunwar D, *et al.* Design of effective catalysts for selective alkyne hydrogenation by doping of ceria with a single-atom promotor. J Am Chem Soc, 2018, 140: 12964–12973
182 Kalaev D, Defferriere T, Nicollet C, *et al.* Dynamic current-voltage analysis of oxygen vacancy mobility in praseodymium-doped ceria over wide temperature limits. Adv Funct Mater, 2020, 30: 1907402
183 Bowman DF, Cemal E, Lehner T, *et al.* Role of defects in determining the magnetic ground state of ytterbium titanate. Nat Commun, 2019, 10: 637
184 Murugappan K, Anderson EM, Teschner D, *et al. Operando* NAP-XPS unveils differences in MoO_3 and Mo_2C during hydrodeoxygenation. Nat Catal, 2018, 1: 960–967
185 Yang J, Bai H, Tan X, *et al.* IR and XPS investigation of visible-light photocatalysis—Nitrogen-carbon-doped TiO_2 film. Appl Surf Sci, 2006, 253: 1988–1994

186 Li J, Zhang M, Guan Z, *et al.* Synergistic effect of surface and bulk single-electron-trapped oxygen vacancy of TiO_2 in the photocatalytic reduction of CO_2. Appl Catal B-Environ, 2017, 206: 300–307
187 Chuvenkova OA, Domashevskaya EP, Ryabtsev SV, *et al.* XANES and XPS investigations of surface defects in wire-like SnO_2 crystals. Phys Solid State, 2015, 57: 153–161
188 Fan W, Li H, Zhao F, *et al.* Boosting the photocatalytic performance of (001) BiOI: enhancing donor density and separation efficiency of photogenerated electrons and holes. Chem Commun, 2016, 52: 5316–5319
189 Xie S, Li M, Wei W, *et al.* Gold nanoparticles inducing surface disorders of titanium dioxide photoanode for efficient water splitting. Nano Energy, 2014, 10: 313–321
190 Guo M, Lu J, Wu Y, *et al.* UV and visible Raman studies of oxygen vacancies in rare-earth-doped ceria. Langmuir, 2011, 27: 3872–3877
191 Zhu G, Zhu J, Li W, *et al.* Tuning the K^+ concentration in the tunnels of α-MnO_2 to increase the content of oxygen vacancy for ozone elimination. Environ Sci Technol, 2018, 52: 8684–8692
192 Jin Y, Long J, Ma X, *et al.* Synthesis of caged iodine-modified ZnO nanomaterials and study on their visible light photocatalytic antibacterial properties. Appl Catal B-Environ, 2019, 256: 117873
193 Elger AK, Hess C. Elucidating the mechanism of working SnO_2 gas sensors using combined *operando* UV/Vis, Raman, and IR spectroscopy. Angew Chem Int Ed, 2019, 58: 15057–15061
194 Zhang N, Li X, Ye H, *et al.* Oxide defect engineering enables to couple solar energy into oxygen activation. J Am Chem Soc, 2016, 138: 8928–8935
195 Tan L, Xu S-, Wang Z, *et al.* Highly selective photoreduction of CO_2 with suppressing H_2 evolution over monolayer layered double hydroxide under irradiation above 600 nm. Angew Chem, 2019, 131: 11986–11993
196 Feng H, Xu Z, Ren L, *et al.* Activating titania for efficient electrocatalysis by vacancy engineering. ACS Catal, 2018, 8: 4288–4293
197 Esch F, Fabris S, Zhou L, *et al.* Electron localization determines defect formation on ceria substrates. Science, 2005, 309: 752–755
198 Zhang YC, Li Z, Zhang L, *et al.* Role of oxygen vacancies in photocatalytic water oxidation on ceria oxide: experiment and DFT studies. Appl Catal B-Environ, 2018, 224: 101–108
199 Shang H, Li M, Li H, *et al.* Oxygen vacancies promoted the selective photocatalytic removal of NO with blue TiO_2 *via* simultaneous molecular oxygen activation and photogenerated hole annihilation. Environ Sci Technol, 2019, 53: 6444–6453
200 Hajiyani H, Pentcheva R. Surface termination and composition control of activity of the $Co_xNi_{1-x}Fe_2O_4$ (001) surface for water oxidation: Insights from DFT+*U* calculations. ACS Catal, 2018, 8: 11773–11782
201 Fan K, Yu J, Ho W. Improving photoanodes to obtain highly efficient dye-sensitized solar cells: a brief review. Mater Horiz, 2017, 4: 319–344
202 Zhang Y, Zhao H, Zhao X, *et al.* Narrow-bandgap Nb_2O_5 nanowires with enclosed pores as high-performance photocatalyst. Sci China Mater, 2019, 62: 203–210
203 Li X, Wen J, Low J, *et al.* Design and fabrication of semiconductor photocatalyst for photocatalytic reduction of CO_2 to solar fuel. Sci China Mater, 2014, 57: 70–100
204 Chen M, Huang Y, Chu W. Exploring a broadened operating pH range for norfloxacin removal *via* simulated solar-light-mediated Bi_2WO_6 process. Chin J Catal, 2019, 40: 673–680
205 Low J, Cheng B, Yu J. Surface modification and enhanced photocatalytic CO_2 reduction performance of TiO_2: a review. Appl Surf Sci, 2017, 392: 658–686
206 Xu B, Zhang Q, Yuan S, *et al.* Synthesis and photocatalytic performance of yttrium-doped CeO_2 with a porous broom-like hierarchical structure. Appl Catal B-Environ, 2016, 183: 361–370
207 Ji G, Yan S, Chen Y, *et al.* Spin injection from ferromagnetic semiconductor CoZnO into ZnO. J Mater Sci Technol, 2008, 24: 415–418
208 Wu F, Cao F, Liu Q, *et al.* Enhancing photoelectrochemical activity with three-dimensional p-CuO/n-ZnO junction photocathodes. Sci China Mater, 2016, 59: 825–832
209 Yoon SH, Han DS, Kang U, *et al.* Effects of electrochemical synthetic conditions on surface property and photocatalytic performance of copper and iron-mixed p-type oxide electrodes. J Mater Sci Tech, 2018, 34: 1503–1510
210 Taylor NT, Davies FH, Davies SG, *et al.* The fundamental mechanism behind colossal permittivity in oxides. Adv Mater, 2019, 31: 1904746
211 Zhang S, Yang H, Huang H, *et al.* Unexpected ultrafast and high adsorption capacity of oxygen vacancy-rich WO_x/C nanowire networks for aqueous Pb^{2+} and methylene blue removal. J Mater Chem A, 2017, 5: 15913–15922
212 Zhang G, Ji Q, Zhang K, *et al.* Triggering surface oxygen vacancies on atomic layered molybdenum dioxide for a low energy consumption path toward nitrogen fixation. Nano Energy, 2019, 59: 10–16
213 Zhou H, Shi Y, Dong Q, *et al.* Surface oxygen vacancy-dependent electrocatalytic activity of $W_{18}O_{49}$ nanowires. J Phys Chem C, 2014, 118: 20100–20106
214 Song JW, Jeon EY, Song DH, *et al.* Multistep enzymatic synthesis of long-chain α,ω-dicarboxylic and ω-hydroxycarboxylic acids from renewable fatty acids and plant oils. Angew Chem Int Ed, 2013, 52: 2534–2537
215 Maiti D, Hare BJ, Daza YA, *et al.* Earth abundant perovskite oxides for low temperature CO_2 conversion. Energy Environ Sci, 2018, 11: 648–659
216 Szlachetko J, Kubas A, Cieślak AM, *et al.* Hidden gapless states during thermal transformations of preorganized zinc alkoxides to zinc oxide nanocrystals. Mater Horiz, 2018, 5: 905–911
217 Vu NN, Kaliaguine S, Do TO. Critical aspects and recent advances in structural engineering of photocatalysts for sunlight-driven photocatalytic reduction of CO_2 into fuels. Adv Funct Mater, 2019, 29: 1901825
218 Choudhury B, Chetri P, Choudhury A. Annealing temperature and oxygen-vacancy-dependent variation of lattice strain, band gap and luminescence properties of CeO_2 nanoparticles. J Exp Nanoscience, 2015, 10: 103–114
219 Sinhamahapatra A, Jeon JP, Kang J, *et al.* Oxygen-deficient zirconia (ZrO_{2-x}): A new material for solar light absorption. Sci Rep, 2016, 6: 27218
220 Kumar S, Ojha AK. Oxygen vacancy induced photoluminescence properties and enhanced photocatalytic activity of ferromagnetic ZrO_2 nanostructures on methylene blue dye under ultra-violet radiation. J Alloys Compd, 2015, 644: 654–662
221 Dong L, Jia R, Xin B, *et al.* Effects of oxygen vacancies on the structural and optical properties of β-Ga_2O_3. Sci Rep, 2017, 7: 40160
222 An S, Zhang G, Wang T, *et al.* High-density ultra-small clusters

and single-atom Fe sites embedded in graphitic carbon nitride (g-C_3N_4) for highly efficient catalytic advanced oxidation processes. ACS Nano, 2018, 12: 9441–9450
223 Ma Z, Li P, Ye L, *et al.* Oxygen vacancies induced exciton dissociation of flexible BiOCl nanosheets for effective photocatalytic CO_2 conversion. J Mater Chem A, 2017, 5: 24995–25004
224 Chen D, Niu F, Qin L, *et al.* Defective $BiFeO_3$ with surface oxygen vacancies: Facile synthesis and mechanism insight into photocatalytic performance. Sol Energy Mater Sol Cells, 2017, 171: 24–32
225 Kim M, Lee B, Ju H, *et al.* Oxygen-vacancy-introduced $BaSnO_{3-\delta}$ photoanodes with tunable band structures for efficient solar-driven water splitting. Adv Mater, 2019, 31: 1903316
226 Hu S, Qiao P, Zhang L, *et al.* Assembly of TiO_2 ultrathin nanosheets with surface lattice distortion for solar-light-driven photocatalytic hydrogen evolution. Appl Catal B-Environ, 2018, 239: 317–323
227 Geng Z, Kong X, Chen W, *et al.* Oxygen vacancies in ZnO nanosheets enhance CO_2 electrochemical reduction to CO. Angew Chem Int Ed, 2018, 57: 6054–6059
228 Ansari SA, Khan MM, Kalathil S, *et al.* Oxygen vacancy induced band gap narrowing of ZnO nanostructures by an electrochemically active biofilm. Nanoscale, 2013, 5: 9238–9246
229 Feng S, Wang T, Liu B, *et al.* Enriched surface oxygen vacancies of photoanodes by photoetching with enhanced charge separation. Angew Chem Int Ed, 2020, 59: 2044–2048
230 Wang H, Zhang W, Li X, *et al.* Highly enhanced visible light photocatalysis and *in situ* FT-IR studies on Bi metal@defective BiOCl hierarchical microspheres. Appl Catal B-Environ, 2018, 225: 218–227
231 Lei F, Sun Y, Liu K, *et al.* Oxygen vacancies confined in ultrathin indium oxide porous sheets for promoted visible-light water splitting. J Am Chem Soc, 2014, 136: 6826–6829
232 Yu H, Li J, Zhang Y, *et al.* Three-in-one oxygen vacancies: whole visible-spectrum absorption, efficient charge separation, and surface site activation for robust CO_2 photoreduction. Angew Chem Int Ed, 2019, 58: 3880–3884
233 Liu S, Yu J, Jaroniec M. Anatase TiO_2 with dominant high-energy {001} facets: Synthesis, properties, and applications. Chem Mater, 2011, 23: 4085–4093
234 Selim S, Pastor E, García-Tecedor M, *et al.* Impact of oxygen vacancy occupancy on charge carrier dynamics in $BiVO_4$ photoanodes. J Am Chem Soc, 2019, 141: 18791–18798
235 Kisiel M, Brovko OO, Yildiz D, *et al.* Mechanical dissipation from charge and spin transitions in oxygen-deficient $SrTiO_3$ surfaces. Nat Commun, 2018, 9: 2946
236 Chikina A, Lechermann F, Husanu MA, *et al.* Orbital ordering of the mobile and localized electrons at oxygen-deficient $LaAlO_3$/$SrTiO_3$ interfaces. ACS Nano, 2018, 12: 7927–7935
237 Anzai H, Takahashi T, Suzuki M, *et al.* Unusual oxygen partial pressure dependence of electrical transport of single-crystalline metal oxide nanowires grown by the vapor-liquid-solid process. Nano Lett, 2019, 19: 1675–1681
238 Ding J, Dai Z, Qin F, *et al.* Z-scheme $BiO_{1-x}Br/Bi_2O_2CO_3$ photocatalyst with rich oxygen vacancy as electron mediator for highly efficient degradation of antibiotics. Appl Catal B-Environ, 2017, 205: 281–291
239 Sun X, Wu J, Li Q, *et al.* Fabrication of $BiOIO_3$ with induced oxygen vacancies for efficient separation of the electron-hole pairs. Appl Catal B-Environ, 2017, 218: 80–90
240 Magyari-Köpe B, Park SG, Lee HD, *et al.* First principles calculations of oxygen vacancy-ordering effects in resistance change memory materials incorporating binary transition metal oxides. J Mater Sci, 2012, 47: 7498–7514
241 Muller DA, Nakagawa N, Ohtomo A, *et al.* Atomic-scale imaging of nanoengineered oxygen vacancy profiles in $SrTiO_3$. Nature, 2004, 430: 657–661
242 Wang B, Zhang M, Cui X, *et al.* Unconventional route to oxygen-vacancy-enabled highly efficient electron extraction and transport in perovskite solar cells. Angew Chem Int Ed, 2020, 59: 1611–1618
243 Jeong J, Aetukuri N, Graf T, *et al.* Suppression of metal-insulator transition in VO_2 by electric field-induced oxygen vacancy formation. Science, 2013, 339: 1402–1405
244 Muñoz-García AB, Pavone M, Carter EA. Effect of antisite defects on the formation of oxygen vacancies in Sr_2FeMoO_6: Implications for ion and electron transport. Chem Mater, 2011, 23: 4525–4536
245 Tang X, Liu X, Zhang L, *et al.* Low crystallinity TiO_2 film with inherent low oxygen vacancy for sensitized solar cells. Chem Phys, 2014, 441: 121–127
246 Wan L, Zhou Q, Wang X, *et al.* Cu_2O nanocubes with mixed oxidation-state facets for (photo)catalytic hydrogenation of carbon dioxide. Nat Catal, 2019, 2: 889–898
247 Kim HS, Jang A, Choi SY, *et al.* Vacancy-induced electronic structure variation of acceptors and correlation with proton conduction in perovskite oxides. Angew Chem Int Ed, 2016, 55: 13499–13503
248 Li H, Qin F, Yang Z, *et al.* New reaction pathway induced by plasmon for selective benzyl alcohol oxidation on BiOCl possessing oxygen vacancies. J Am Chem Soc, 2017, 139: 3513–3521
249 Tanveer M, Wu Y, Qadeer MA, *et al.* Atypical $BiOCl/Bi_2S_3$ hetero-structures exhibiting remarkable photo-catalyst response. Sci China Mater, 2018, 61: 101–111
250 Zhou Z, Liu J, Long R, *et al.* Control of charge carriers trapping and relaxation in hematite by oxygen vacancy charge: *Ab initio* non-adiabatic molecular dynamics. J Am Chem Soc, 2017, 139: 6707–6717
251 Gan J, Lu X, Wu J, *et al.* Oxygen vacancies promoting photoelectrochemical performance of In_2O_3 nanocubes. Sci Rep, 2013, 3: 1021
252 Li L, Feng X, Nie Y, *et al.* Insight into the effect of oxygen vacancy concentration on the catalytic performance of MnO_2. ACS Catal, 2015, 5: 4825–4832
253 Liu B, Li C, Zhang G, *et al.* Oxygen vacancy promoting dimethyl carbonate synthesis from CO_2 and methanol over Zr-doped CeO_2 nanorods. ACS Catal, 2018, 8: 10446–10456
254 Wang Q, Chen L, Guan S, *et al.* Ultrathin and vacancy-rich CoAl-layered double hydroxide/graphite oxide catalysts: promotional effect of cobalt vacancies and oxygen vacancies in alcohol oxidation. ACS Catal, 2018, 8: 3104–3115
255 Nie L, Yu J, Jaroniec M, *et al.* Room-temperature catalytic oxidation of formaldehyde on catalysts. Catal Sci Technol, 2016, 6: 3649–3669
256 Goulas KA, Mironenko AV, Jenness GR, *et al.* Fundamentals of C–O bond activation on metal oxide catalysts. Nat Catal, 2019, 2: 269–276
257 Setvin M, Reticcioli M, Poelzleitner F, *et al.* Polarity compensation mechanisms on the perovskite surface $KTaO_3$ (001). Science, 2018, 359: 572–575
258 Bobadilla LF, Santos JL, Ivanova S, *et al.* Unravelling the role of

oxygen vacancies in the mechanism of the reverse water–gas shift reaction by *operando* DRIFTS and ultraviolet–visible spectroscopy. ACS Catal, 2018, 8: 7455–7467
259 Varandili SB, Huang J, Oveisi E, *et al.* Synthesis of Cu/CeO_{2-x} nanocrystalline heterodimers with interfacial active sites to promote CO_2 electroreduction. ACS Catal, 2019, 9: 5035–5046
260 Martin O, Martín AJ, Mondelli C, *et al.* Indium oxide as a superior catalyst for methanol synthesis by CO_2 hydrogenation. Angew Chem Int Ed, 2016, 55: 6261–6265
261 Ji Y, Luo Y. New mechanism for photocatalytic reduction of CO_2 on the anatase TiO_2 (101) surface: The essential role of oxygen vacancy. J Am Chem Soc, 2016, 138: 15896–15902
262 Li H, Li J, Ai Z, *et al.* Oxygen vacancy-mediated photocatalysis of BiOCl: reactivity, selectivity, and perspectives. Angew Chem Int Ed, 2018, 57: 122–138
263 Huang S, Zhu X, Cheng B, *et al.* Flexible nickel foam decorated with Pt/NiO nanoflakes with oxygen vacancies for enhanced catalytic formaldehyde oxidation at room temperature. Environ Sci-Nano, 2017, 4: 2215–2224
264 Heisig T, Baeumer C, Gries UN, *et al.* Oxygen exchange processes between oxide memristive devices and water molecules. Adv Mater, 2018, 30: 1800957
265 Li H, Shang J, Ai Z, *et al.* Efficient visible light nitrogen fixation with BiOBr nanosheets of oxygen vacancies on the exposed {001} facets. J Am Chem Soc, 2015, 137: 6393–6399
266 Wang S, Hai X, Ding X, *et al.* Light-switchable oxygen vacancies in ultrafine Bi_5O_7Br nanotubes for boosting solar-driven nitrogen fixation in pure water. Adv Mater, 2017, 29: 1701774
267 Yang X, Wang S, Yang N, *et al.* Oxygen vacancies induced special CO_2 adsorption modes on Bi_2MoO_6 for highly selective conversion to CH_4. Appl Catal B-Environ, 2019, 259: 118088
268 Wang M, Shen M, Jin X, *et al.* Oxygen vacancy generation and stabilization in CeO_{2-x} by Cu introduction with improved CO_2 photocatalytic reduction activity. ACS Catal, 2019, 9: 4573–4581
269 Jia H, Du A, Zhang H, *et al.* Site-selective growth of crystalline ceria with oxygen vacancies on gold nanocrystals for near-infrared nitrogen photofixation. J Am Chem Soc, 2019, 141: 5083–5086
270 Li C, Wang T, Zhao ZJ, *et al.* Promoted fixation of molecular nitrogen with surface oxygen vacancies on plasmon-enhanced TiO_2 photoelectrodes. Angew Chem Int Ed, 2018, 57: 5278–5282
271 Duan C, Li F, Zhang H, *et al.* Template synthesis of hierarchical porous metal–organic frameworks with tunable porosity. RSC Adv, 2017, 7: 52245–52251
272 Tan S, Ji Y, Zhao Y, *et al.* Molecular oxygen adsorption behaviors on the rutile TiO_2 (110)-1×1 surface: An *in situ* study with low-temperature scanning tunneling microscopy. J Am Chem Soc, 2011, 133: 2002–2009
273 Zhang J, Yin R, Shao Q, *et al.* Oxygen vacancies in amorphous InO_x nanoribbons enhance CO_2 adsorption and activation for CO_2 electroreduction. Angew Chem Int Ed, 2019, 58: 5609–5613
274 Huygh S, Bogaerts A, Neyts EC. How oxygen vacancies activate CO_2 dissociation on TiO_2 anatase (001). J Phys Chem C, 2016, 120: 21659–21669
275 Tanabe Y, Nishibayashi Y. Developing more sustainable processes for ammonia synthesis. Coord Chem Rev, 2013, 257: 2551–2564
276 Jia HP, Quadrelli EA. Mechanistic aspects of dinitrogen cleavage and hydrogenation to produce ammonia in catalysis and organometallic chemistry: relevance of metal hydride bonds and dihydrogen. Chem Soc Rev, 2014, 43: 547–564
277 Han Z, Choi C, Hong S, *et al.* Activated TiO_2 with tuned vacancy for efficient electrochemical nitrogen reduction. Appl Catal B-Environ, 2019, 257: 117896
278 Jiang Z, Sun H, Wang T, *et al.* Nature-based catalyst for visible-light-driven photocatalytic CO_2 reduction. Energy Environ Sci, 2018, 11: 2382–2389
279 Lukashuk L, Yigit N, Rameshan R, *et al.* *Operando* insights into CO oxidation on cobalt oxide catalysts by NAP-XPS, FTIR, and XRD. ACS Catal, 2018, 8: 8630–8641
280 Li H, Shang J, Zhu H, *et al.* Oxygen vacancy structure associated photocatalytic water oxidation of BiOCl. ACS Catal, 2016, 6: 8276–8285
281 Staykov A, Téllez H, Akbay T, *et al.* Oxygen activation and dissociation on transition metal free perovskite surfaces. Chem Mater, 2015, 27: 8273–8281
282 Lee S, Jin W, Kim SH, *et al.* Oxygen vacancy diffusion and condensation in lithium-ion battery cathode materials. Angew Chem, 2019, 131: 10588–10595
283 Schmitt R, Nenning A, Kraynis O, *et al.* A review of defect structure and chemistry in ceria and its solid solutions. Chem Soc Rev, 2020, 49: 554–592
284 Frei MS, Mondelli C, Cesarini A, *et al.* Role of zirconia in indium oxide-catalyzed CO_2 hydrogenation to methanol. ACS Catal, 2019, 10: 1133–1145
285 Tsoukalou A, Abdala PM, Stoian D, *et al.* Structural evolution and dynamics of an In_2O_3 catalyst for CO_2 hydrogenation to methanol: an *operando* XAS-XRD and *in situ* TEM study. J Am Chem Soc, 2019, 141: 13497–13505
286 Hirakawa H, Hashimoto M, Shiraishi Y, *et al.* Photocatalytic conversion of nitrogen to ammonia with water on surface oxygen vacancies of titanium dioxide. J Am Chem Soc, 2017, 139: 10929–10936
287 Wang Y, Oord R, van den Berg D, *et al.* Oxygen vacancies in reduced Rh/ and Pt/ceria for highly selective and reactive reduction of NO into N_2 in excess of O_2. ChemCatChem, 2017, 9: 2935–2938
288 Gao S, Sun Z, Liu W, *et al.* Atomic layer confined vacancies for atomic-level insights into carbon dioxide electroreduction. Nat Commun, 2017, 8: 14503
289 Gao P, Li S, Bu X, *et al.* Direct conversion of CO_2 into liquid fuels with high selectivity over a bifunctional catalyst. Nat Chem, 2017, 9: 1019–1024
290 Nong S, Dong W, Yin J, *et al.* Well-dispersed ruthenium in mesoporous crystal TiO_2 as an advanced electrocatalyst for hydrogen evolution reaction. J Am Chem Soc, 2018, 140: 5719–5727
291 Jehannin M, Rao A, Cölfen H. New horizons of nonclassical crystallization. J Am Chem Soc, 2019, 141: 10120–10136
292 Petel BE, Brennessel WW, Matson EM. Oxygen-atom vacancy formation at polyoxovanadate clusters: homogeneous models for reducible metal oxides. J Am Chem Soc, 2018, 140: 8424–8428
293 Hu X, Zhang Y, Wang B, *et al.* Novel g-C_3N_4/$BiOCl_xI_{1-x}$ nanosheets with rich oxygen vacancies for enhanced photocatalytic degradation of organic contaminants under visible and simulated solar light. Appl Catal B-Environ, 2019, 256: 117789
294 Xie Z, Zhou J, Wang J, *et al.* Oxygen-atom vacancy formation at polyoxovanadate clusters: homogeneous models for reducible metal oxides. Appl Catal B-Environ, 2019, 253: 28–40
295 Liu Y, Miao C, Yang P, *et al.* Synergetic promotional effect of oxygen vacancy-rich ultrathin TiO_2 and photochemical induced highly dispersed Pt for photoreduction of CO_2 with H_2O. Appl

Catal B-Environ, 2019, 244: 919–930
296 Chen J, Iyemperumal SK, Fenton T, *et al.* Synergy between defects, photoexcited electrons, and supported single atom catalysts for CO_2 reduction. ACS Catal, 2018, 8: 10464–10478
297 Wu SM, Liu XL, Lian XL, *et al.* Homojunction of oxygen and titanium vacancies and its interfacial n-p effect. Adv Mater, 2018, 30: 1802173
298 Hegner FS, Forrer D, Galán-Mascarós JR, *et al.* Versatile nature of oxygen vacancies in bismuth vanadate bulk and (001) surface. J Phys Chem Lett, 2019, 10: 6672–6678
299 Wang Y, Cai J, Wu M, *et al.* Rational construction of oxygen vacancies onto tungsten trioxide to improve visible light photocatalytic water oxidation reaction. Appl Catal B-Environ, 2018, 239: 398–407
300 Chen Y, Cao X, Lin B, *et al.* Origin of the visible-light photoactivity of NH_3-treated TiO_2: Effect of nitrogen doping and oxygen vacancies. Appl Surf Sci, 2013, 264: 845–852
301 Zhang X, Fan C, Wang Y, *et al.* DFT+U predictions: The effect of oxygen vacancy on the structural, electronic and photocatalytic properties of Mn-doped BiOCl. Comput Mater Sci, 2013, 71: 135–145
302 Weaver JF, Zhang F, Pan L, *et al.* Vacancy-mediated processes in the oxidation of CO on PdO(101). Acc Chem Res, 2015, 48: 1515–1523
303 Jiang Y, Ning H, Tian C, *et al.* Single-crystal TiO_2 nanorods assembly for efficient and stable cocatalyst-free photocatalytic hydrogen evolution. Appl Catal B-Environ, 2018, 229: 1–7
304 Wang J, Liu J, Zhang B, *et al.* Stabilizing the oxygen vacancies and promoting water-oxidation kinetics in cobalt oxides by lower valence-state doping. Nano Energy, 2018, 53: 144–151

Acknowledgements This work was financially supported by the National Natural Science Foundation of China (U1905215, 51772053 and 51672046).

Author contributions Zhuang Z and Yu Y conceptualized the work, and wrote and revised the manuscript. Zhuang G and Chen Y collected and summarized the literatures, and contributed to the manuscript writing. Yu J revised the manuscript and offered creative proposal for improving the depth and coverage of the review. All authors contributed to the general discussion.

Conflict of interest The authors declare no conflict of interest.

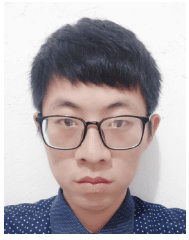

Guoxin Zhuang received his BSc in materials science and engineering from Fuzhou University. He is currently pursuing his PhD degree at Fuzhou University under the supervision of Prof. Yu and Prof. Zhuang. His research focuses on the design of MOFs and catalysts for CO_2 photoreduction.

Zanyong Zhuang received his BSc in chemistry from Xiamen University, and his PhD in 2011 from Fujian Institute of Research on the Structure of Matter (FJIRSM), Chinese Academy of Sciences (CAS). He became an associate researcher in FJIRSM, CAS in 2014. Currently he is an associate professor at Fuzhou University. His research interests include the design of low-dimensional nanostructures, nanocrystals growth and assembly, comprehensive utilization of solid waste, and the related catalytic topics.

Yan Yu received her BSc, MSc and PhD degrees from Fuzhou University. She was a postdoctoral fellow in FJIRSM, CAS, and became a Professor at Fuzhou University in 2011. Her research interests include semiconductors, photocatalysis, environmental purification materials, comprehensive utilization of solid waste, and the related topics.

Jiaguo Yu received his BSc and MSc degrees in chemistry from the Central China Normal University and Xi'an Jiaotong University, respectively, and his PhD in materials science in 2000 from Wuhan University of Technology. In 2000, he became a Professor at Wuhan University of Technology. He was a postdoctoral fellow at the Chinese University of Hong Kong from 2001 to 2004, a visiting scientist from 2005 to 2006 at the University of Bristol, and a visiting scholar from 2007 to 2008 at the University of Texas, Austin. His research interests include semiconductors, photocatalysis, photocatalytic hydrogen production, solar fuels, dye-sensitized solar cells, adsorption, CO_2 capture, graphene, and the related topics.

金属氧化物中的氧空位: 先进催化剂设计的新进展

庄国鑫[1,2], 陈雅文[1,2], 庄赞勇[1,2*], 于岩[1,2*], 余家国[3*]

摘要 高效、稳定的催化材料有望解决日益严峻的环境污染和能源危机问题. 金属氧化物具有高稳定性、低成本以及高催化活性等优点, 在能源转换和环境净化等领域有广阔的应用前景, 已广泛应用于H_2O裂解、CO_2还原、固氮以及污染物的高级氧化等催化领域中. 氧空位作为金属氧化物中普遍存在的一种内在缺陷, 被证实可显著影响甚至改变材料的物理化学性质, 是调控催化剂结构和催化性能的有效手段. 深入了解催化材料氧空位的调节以及氧空位对催化性能的作用机制, 为设计出高效金属氧化物催化剂提供重要理论基础. 本文综述了近年来调控氧空位的基本原理和控制因素, 介绍了氧空位的结构与催化活性的基本关系, 包括如何影响材料的光吸收、电荷分离和反应物的吸附活化等, 着重介绍了氧空位的形成机制及其对金属氧化物催化特性的影响. 同时, 我们还对多组分催化过程中, 氧空位与其他类型催化组分间的协同催化机制进行了总结. 最后, 本文提出了材料缺陷工程在催化领域面临的机遇和挑战.

